

Full length article

Flux and genesis of CO₂ degassing from volcanic-geothermal fields of Gulu-Yadong rift in the Lhasa terrane, South Tibet: Constraints on characteristics of deep carbon cycle in the India-Asia continent subduction zone



Lihong Zhang^a, Zhengfu Guo^{a,*}, Yuji Sano^b, Maoliang Zhang^a, Yutao Sun^a, Zhihui Cheng^a, Tsanyao Frank Yang^c

^a Key Laboratory of Cenozoic Geology and Environment, Institute of Geology and Geophysics, Chinese Academy of Sciences, Beijing 100029, China

^b Atmosphere and Ocean Research Institute, University of Tokyo, Kashiwanoha, Chiba 277-8564, Japan

^c Department of Geosciences, National Taiwan University, Taipei 10699, Taiwan

ARTICLE INFO

Keywords:

CO₂ degassing
He-C coupling model
India-Asia continent subduction zone
Gulu-Yadong rift
South Tibet

ABSTRACT

Gulu-Yadong rift (GYR) is the longest extensional, NE-SW-trending rift in the Himalayas and Lhasa terrane of South Tibet. Many volcanic-geothermal fields (VGFs), which comprise intense hot springs, steaming fissures, geysers and soil micro-seepage, are distributed in the GYR, making it ideal area for studying deep carbon emissions in the India-Asia continent subduction zone. As for the northern segment of GYR in the Lhasa terrane, its total flux and genesis of CO₂ emissions are poorly understood. Following accumulation chamber method, soil CO₂ flux survey has been carried out in VGFs (i.e., Jidaguo, Ningzhong, Sanglai, Tuoma and Yuzhai from south to north) of the northern segment of GYR. Total soil CO₂ output of the northern GYR is about $1.50 \times 10^7 \text{ t a}^{-1}$, which is attributed to biogenic and volcanic-geothermal source. Geochemical characteristics of the volcanic-geothermal gases (including CO₂ and He) of the northern GYR indicate their significant mantle-derived affinities. Combined with previous petrogeochemical and geophysical data, our He-C isotope modeling calculation results show that (1) excess mantle-derived ³He reflects degassing of volatiles related with partial melts from enriched mantle wedge induced by northward subduction of the Indian lithosphere, and (2) the crust-mantle interaction can provide continuous heat and materials for the overlying volcanic-geothermal system, in which magma-derived volatiles are inferred to experience significant crustal contamination during their migration to the surface.

1. Introduction

Volcanic-geothermal activities at convergent and divergent plate boundaries have been the focus of global carbon budget and Earth degassing in recent years (Burton et al., 2013; Zhang, 2014; Kelemen and Manning, 2015). Compared with the well-established database of carbon emissions and chemical geodynamics of volatiles from mid-ocean ridge (Graham, 2002; Resing et al., 2004; Burley and Katz, 2015) and oceanic subduction zone (Sano and Marty, 1995; Hilton et al., 2002; Sano and Fischer, 2013), flux and genesis of deep carbon cycle in continent subduction zone remains poorly understood. For this reason, the present volcanic-geothermal activities in continent subduction zone have drawn growing attention from studies on geological carbon emissions (Newell et al., 2008; Zhang et al., 2014).

Northward subduction of the Indian continental lithosphere beneath South Tibet has been demonstrated by evidence from occurrence of the

ultrahigh-pressure metamorphic rocks (Hacker et al., 2005; Donaldson et al., 2013), seismic tomography data (Nábělek et al., 2009; Zhao et al., 2011; Liang et al., 2016), plate-tectonic reconstructions (DeCelles et al., 2011) and post-collisional K-rich magmatic rocks (Guo et al., 2015; Wang et al., 2015; Liu et al., 2017). As a result of the continental collision and subsequent subduction of the Indian plate, near N-S-trending, lithospheric extension-related rift occurred in South Tibet (Tian et al., 2015; Huang et al., 2016), where extensive post-collisional volcanic rocks (Guo et al., 2013; Zhang et al., 2017a) and present-day volcanic-geothermal activities (Yokoyama et al., 1999; Hoke et al., 2000) are exposed (Fig. 1a). These extensional-induced rift systems provide ideal study sites for understanding the scale and mechanism of geological carbon emissions in the India-Asia continent subduction zone.

The near NE-SW-trending Gulu-Yadong rift (Fig. 1), formed by lithospheric extension since Miocene (12–5 Ma; Harrison et al., 1995; Yin and Harrison, 2000; Wang et al., 2014), extends about 500 km from

* Corresponding author at: No. 19, Beitucheng Western Road, Chaoyang District, Beijing 100029, China.
E-mail address: zfguo@mail.iggcas.ac.cn (Z. Guo).

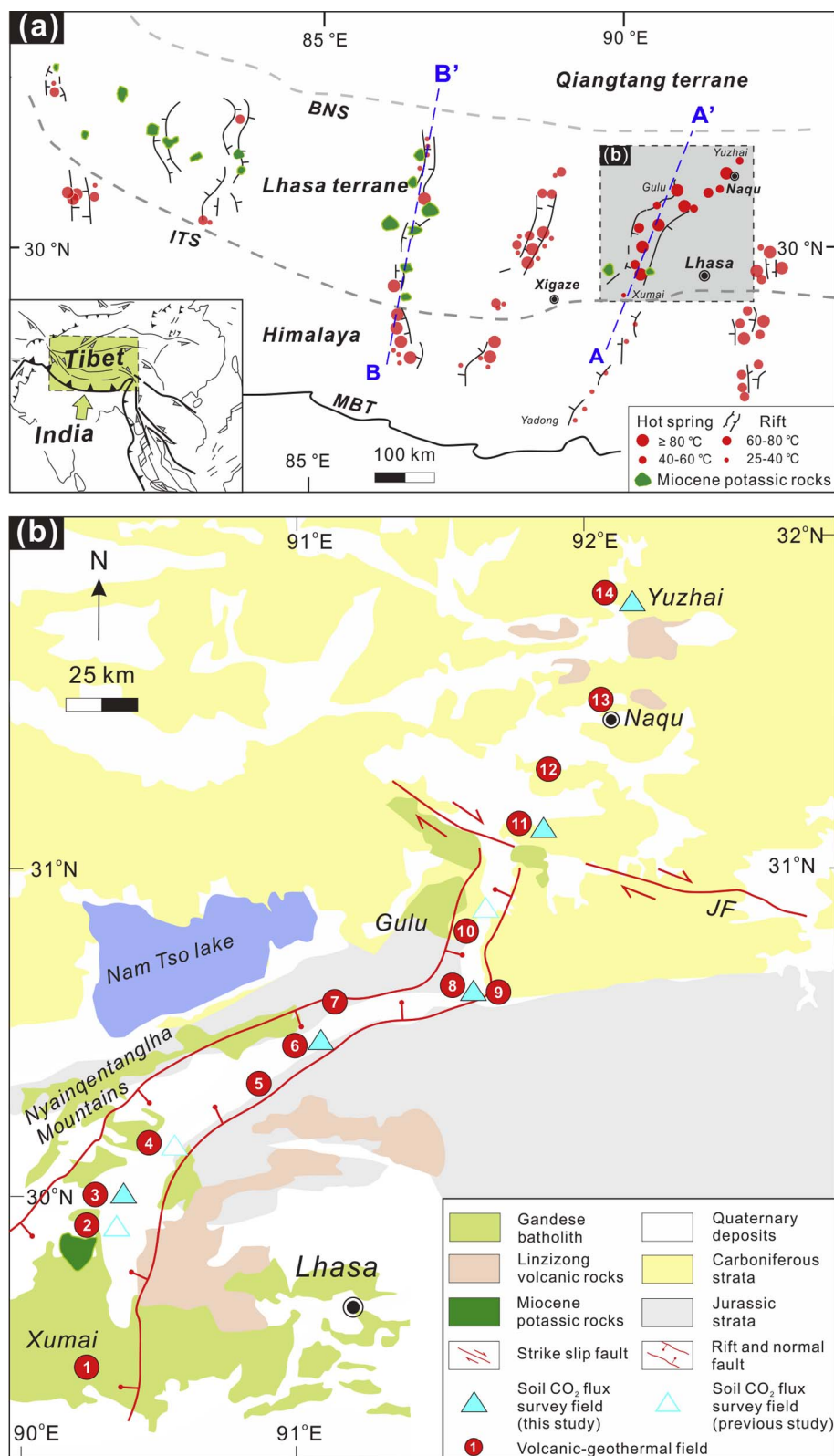


Fig. 1. (a) Simplified geological map showing distribution of the hydrothermal activities in South Tibet (modified from Armijo et al. (1986), Guo et al. (2015), Zhang et al. (2017b)). Abbreviations: ITS, Indus-Tsangpo suture; BNS, Bangong-Nujiang suture; MBT, main boundaries thrust. Cross section AA' and BB' are shown in Figs. 6 and 7. (b) Simplified geological map showing the volcanic-geothermal fields (VGFs) and the Cenozoic magmatism along the Gulu-Yadong rift (modified from Kapp et al. (2005), Liu (2014), Weller et al. (2016)). JF, Jiali fault. Numbers indicate the VGFs: 1, Xumai; 2, Yangying; 3, Jidaguo; 4, Yangbajing; 5, Laduogang; 6, Ningzhong; 7, Yuela; 8, Sanglai; 9, Jiaqiong; 10, Gulu; 11, Tuoma; 12, Luoma; 13, Naqu; 14, Yuzhai.

Gulu (about 31°10'N; Armijo et al., 1986) in the Lhasa terrane to Yadong (about 27°29'N) in the Himalayas. The GYR is characterized by extensively distributed hydrothermal activities, such as soil micro-seepage, fumaroles, steaming fissures, hot springs and hydrothermal explosions (Fig. 2; Yokoyama et al., 1999; Zhao et al., 2002). These hydrothermal activities suggest significant geological carbon output from extensional rift systems in the India-Asia continent subduction zone, but

only a few studies have been done so far (Chiodini et al., 1998; Zhang et al., 2014, 2017b). Additionally, previous studies (e.g., Yokoyama et al., 1999; Hoke et al., 2000; Newell et al., 2008) have identified a domain of mantle-derived helium emissions in northern segment of the GYR (Fig. 1a), i.e., the GYR in the Lhasa terrane. Nevertheless, the flux and genesis of deep carbon and properties of the mantle source should be further constrained for hydrothermal volatiles released from the

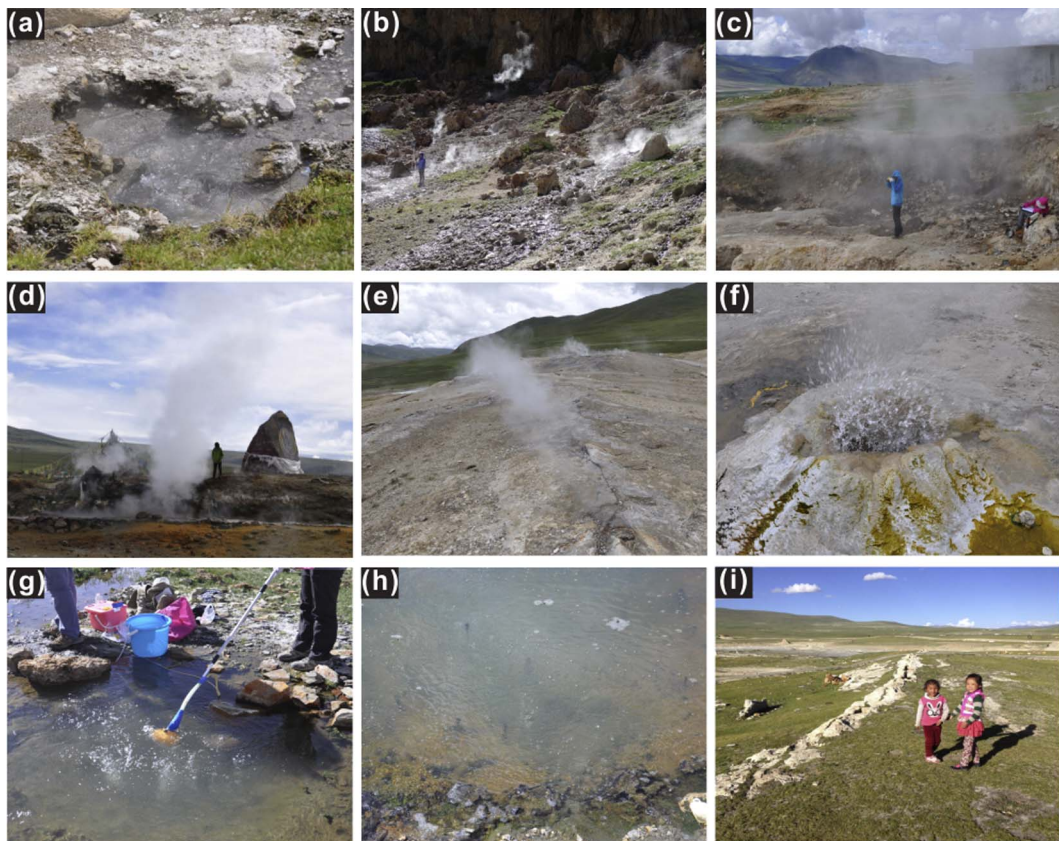


Fig. 2. Forms of gas-releasing from the hydrothermal activities along GYR (a) Boiling hot spring from Yangying; (b) Soil micro-seepage and hot springs from Yangying; (c) Soil micro-seepage from Yangbajing; (d) Soil micro-seepage and hot springs from Ningzhong; (e) Steaming fissure from Gulu; (f) Geyser from Gulu; (g) Bubbles springs from Luoma; (h) Bubbles springs from Tuoma; (i) Residual siliceous sinter or travertine with no active hydrothermal manifestations from Yuzhai.

northern GYR, especially considering the geodynamic setting of the Indian continent subduction beneath South Tibet.

In this study, we report in-situ field measured data of soil CO₂ fluxes for selected VGFs in northern segment of the GYR, in order to understand characteristics and mechanism of deep carbon emissions from extensional rift systems in the India-Asia continent subduction zone. It should be noted that, although active volcanoes are absent in South Tibet, the investigated areas are classified as VGFs, because the source of heat and materials of the hydrothermal activities may be provided by magmatic system beneath the northern segment of GYR (Zhang et al., 2017a, 2017b). Combined with constraints from petrogeochemical (e.g., Guo et al., 2013, 2015; Zhang et al., 2017b) and geophysical (e.g., Nelson et al., 1996; Xie et al., 2016) studies, we estimate the flux of CO₂ degassing from the northern segment of GYR and propose a robust model to understand the mechanism of deep carbon cycle in the India-Asia continent subduction zone.

2. Geological setting

The Lhasa terrane is located in southern part of the Tibetan Plateau (Fig. 1a), which is separated from the Qiangtang terrane to the north by the Bangong-Nujiang suture (BNS) and from the Himalayas to the south by the Indus-Tsangpo suture (ITS). Precambrian basement rocks have been discovered in central and northern Lhasa terrane, as represented by the Proterozoic metamorphic rocks to the west of the Nam Tso lake ~ 750 Ma; Hu et al., 2005) and the Amdo gneiss (852 Ma; Guynn et al., 2006). Paleozoic to Mesozoic sedimentary strata (e.g., limestone; Kapp et al., 2005), together with Jurassic to Cretaceous volcanic-sedimentary sequences, comprise the sedimentary cover in the Lhasa terrane (Zhu et al., 2008). During Late Cretaceous and Cenozoic times, magmatic activities have become significant in South Tibet. The representative

magmatic rocks include the Gangdese batholith, the Linzizong volcanic rocks and post-collisional potassium-rich volcanic rocks and adakites (Guo et al., 2007; Ji et al., 2012; Lee et al., 2012; Wang et al., 2015).

Large-scale high-angle normal faults separate the northern GYR from the high-elevation mountain ranges on both sides of the rift (Harrison et al., 1995; Zhang et al., 2013), such as the NE-SW-trending Nyainqentanghla Mountain (Fig. 1b). Variable scales of faults and fractures are widely distributed in GYR (Armijo et al., 1986), together with the high-angle normal faults, forming an interconnected fault system in the leading edge of the India-Asia continent subduction zone. Cover rocks of the northern GYR are mainly composed of Carboniferous shallow marine clastic deposits and limestones (Kapp et al., 2005), Cretaceous to Tertiary granitoids (Kidd et al., 1988; Kapp et al., 2005; Weller et al., 2016), Paleocene to Eocene volcanic sequences of the Linzizong Formation (Coulon et al., 1986) and Quaternary sediments with various origin (e.g., glacial, alluvial, fluvial, and lacustrine; Armijo et al., 1986; Kapp et al., 2005).

As shown in Fig. 1b, there is a hydrothermal belt composed of fourteen VGFs in our study area, extending from Xumai in the south to Yuzhai in the north. Most of them (i.e., those to the south of Gulu) are located in the northern segment of GYR, and can be taken as on-rift VGFs (Armijo et al., 1986). In contrast, those to the north of Gulu are away from GYR and thus can be taken as off-rift VGFs (Fig. 1b; Armijo et al., 1986). It is noted that hydrothermal activities in the on-rift VGFs appear to be more intense than those in the off-rift VGFs. For example, the on-rift VGFs are characterized by the highest fluid temperature of > 80 °C (Tables 1 and 2) and the occurrence of boiling hot springs (Fig. 2a and b), steaming ground or fissures (Fig. 2c–e) and geysers (Fig. 2f), while the off-rift VGFs have relatively lower fluid temperatures (Tables 1 and 2) and less intense hydrothermal activities (Fig. 2g–i).

Table 1
Chemical compositions of the volcanic-geothermal gases in the northern segment of GYR.

Field no.	Fields	Sample No.	Gas types	T(°C)	N ₂ (%)	O ₂ (%)	CO ₂ (%)	CH ₄ (%)	H ₂ (%)	Ar (%)	He (ppm)	N ₂ /Ar	N ₂ /He
1	Xumai	XM1501	Bubble gas	26.6	91.4	0.06	0.65	6.04	n.d.	0.83	9813	110	93.2
1	Xumai	XM1502	Bubble gas	26.2	89.9	0.05	0.83	7.19	0.25	0.82	9821	110	91.5
2	Yangying	YY1501	Bubble gas	82.1	15.0	3.31	81.1	0.11	0.14	0.34	135	44.6	1113
5	Laduogang	LDG1501	Bubble gas	22.7	1.79	0.76	97.1	0.30	n.d.	0.05	0.38	34.2	47,080
5	Laduogang	LDG1502	Bubble gas	53.3	2.04	0.89	96.8	0.23	n.d.	0.05	1.79	37.9	11,369
6	Ningzhong	NZ1501	Bubble gas	60.7	12.2	1.22	86.4	0.07	n.d.	0.12	690	99.8	176
6	Ningzhong	NZ1502	Bubble gas	59.7	1.88	0.95	97.1	n.d.	n.d.	0.05	1.73	36.9	10,888
7	Yuela	YL1501	Bubble gas	66.2	2.58	1.24	96.1	0.01	n.d.	0.07	0.75	36.5	34,384
8	Sanglai	SL1501	Bubble gas	82.9	3.51	1.54	94.9	n.d.	n.d.	0.07	3.00	47.7	11,708
8	Sanglai	SL1502	Bubble gas	80.8	3.58	1.59	94.7	n.d.	n.d.	0.08	2.63	42.7	13,610
9	Jiaqiong	JQ1501	Bubble gas	41.5	1.86	0.93	97.2	n.d.	n.d.	0.05	3.11	37.0	5980
11	Tuoma	TM1501	Bubble gas	47.7	2.27	1.30	96.4	n.d.	n.d.	0.06	4.08	37.6	5572
11	Tuoma	TM1502	Bubble gas	50.9	1.68	0.80	97.4	0.05	n.d.	0.05	4.92	36.3	3412
12	Luoma	LM1501	Bubble gas	25.7	4.41	0.66	94.8	0.01	n.d.	0.12	41.6	37.0	1061
14	Yuzhai	YZ1501	Bubble gas	50.9	4.52	2.00	93.4	0.01	n.d.	0.10	7.72	46.4	5857
14	Yuzhai	YZ1502	Bubble gas	49.6	4.79	1.69	93.4	0.01	n.d.	0.09	7.21	54.1	6639

3. Samples and analytical methods

3.1. Soil CO₂ flux measurement

On the basis of soil CO₂ flux survey in previous studies (Zhang et al., 2014, 2017b), five VGFs (Fig. 1b), approximately 4200–4700 m above sea level, were chosen as study areas for soil CO₂ flux survey (see details in the Supplementary Table S1). In particular, two off-rift VGFs (i.e., Tuoma and Yuzhai; Fig. 1b) were studied, aiming to compare main factors that control the variation of the soil CO₂ fluxes in South Tibet. Accumulation chamber method and portable infra-red CO₂ analyzer (GXH-3010E) were used to measure the soil CO₂ flux (257 points) during July 2015. Two factors should be considered during the in-situ field measurement of soil CO₂ flux: (1) only the regions with less influence from vegetation and human activities were selected, with inter-measurement point by 50–100 m intervals; (2) the edge of cylindrical chamber must be covered with soil and sealed well during measurement, in order to prevent from contamination of the air (Lan et al., 2007). The detailed measurement and calculation procedures are described in Chiodini et al. (1998) and Zhang et al. (2014).

Table 2
Helium and carbon ratios of the volcanic-geothermal gases in GYR.

Field no.	Locality	Sample no.	Gas type	Latitude (degree)	Longitude (degree)	Elevation (m)	T (°C)	δ ¹³ C (‰)	CO ₂ / ³ He	(⁴ He/ ²⁰ Ne) _M	R _M /R _A	±	X	R _C /R _A
1	Xumai	XM1501	Bubble gas	29°27'37.5"	90°15'23.2"	3899	26.6	-14.8	1.11 × 10 ⁷	193	0.04	0.029	760	0.04
1	Xumai	XM1502	Bubble gas	29°27'34.5"	90°15'26.8"	3917	26.2	-14.6	6.39 × 10 ⁶	1146	0.10	0.005	4511	0.09
2	Yangying	YY1501	Bubble gas	29°44'24.3"	90°22'10.7"	4737	82.1	-4.96	5.04 × 10 ¹⁰	26.5	0.09	0.002	104	0.08
3	Jidaguo	JDG1501	Dissolved gas	29°50'43.7"	90°17'18.2"	4609	55.8			108	0.08	0.007	425	0.07
5	Laduogang	LDG1501	Bubble gas	30°11'59.1"	90°36'0.5"	4559	22.7	-7.05	3.51 × 10 ¹²	0.81	0.52	0.137	3.18	0.33
5	Laduogang	LDG1502	Bubble gas	30°11'59.6"	90°35'59"	4558	53.3	-6.94	1.16 × 10 ¹²	3.7	0.33	0.04	14.6	0.28
6	Ningzhong	NZ1501	Bubble gas	30°24'44.3"	90°56'34.6"	4247	60.7	-3.56	2.96 × 10 ⁹	325	0.30	0.165	1278	0.30
6	Ningzhong	NZ1502	Bubble gas	30°24'44.5"	90°56'35.1"	4247	59.7	-6.37	8.96 × 10 ¹¹	3.09	0.45	0.014	12.2	0.40
7	Yuela	YL1501	Bubble gas	30°37'14.9"	91°14'01.8"	4546	66.2	-3.01	1.89 × 10 ¹²	1.25	0.49	0.137	4.92	0.36
8	Sanglai	SL1501	Bubble gas	30°40'1.1"	91°35'24.8"	4499	82.9	-2.19	1.13 × 10 ¹²	5.91	0.20	0.019	23.3	0.16
8	Sanglai	SL1502	Bubble gas	30°39'59.9"	91°35'26.3"	4499	80.8	-4.27	1.44 × 10 ¹²	4.15	0.18	0.043	16.3	0.12
9	Jiaqiong	JQ1501	Bubble gas	30°38'53.4"	91°35'44.3"	4490	41.5	-3.86	2.18 × 10 ¹¹	6.13	1.02	0.158	24.1	1.02
11	Tuoma	TM1501	Bubble gas	31°09'37.2"	91°50'58.3"	4671	47.7	-2.88	2.48 × 10 ¹¹	8.2	0.68	0.122	32.3	0.67
11	Tuoma	TM1502	Bubble gas	31°09'37.3"	91°50'56.8"	4662	50.9	-4.08	5.62 × 10 ¹¹	1.51	0.25	0.014	5.94	0.11
12	Luoma	LM1501	Bubble gas	31°17'58.6"	91°52'23.6"	4548	25.7	-5.17	9.43 × 10 ¹⁰	68.3	0.17	0.004	269	0.17
14	Yuzhai	YZ1501	Bubble gas	31°44'38"	92°05'58.3"	4647	50.9	-0.10	3.91 × 10 ¹¹	9.95	0.22	0.02	39.2	0.20
14	Yuzhai	YZ1502	Bubble gas	31°44'39"	92°06'0.5"	4650	49.6	-0.49	5.44 × 10 ¹¹	12.7	0.17	0.012	50	0.15

(1) R_M/R_A is the measured ³He/⁴He ratio divided by the ³He/⁴He ratio in air (R_A = 1.39 × 10⁻⁶; Sano and Wakita, 1985).

(2) X = (⁴He/²⁰Ne)_M/(⁴He/²⁰Ne)_{air} × β_{Ne}/β_{He}, where β represent Bunsen coefficients assuming a groundwater recharge temperature of 15 °C (β_{Ne}/β_{He} = 0.82, Weiss, 1971), (⁴He/²⁰Ne)_M is the measured ratio and (⁴He/²⁰Ne)_{air} is the ratio of the air (0.32, Sano and Wakita, 1985).

(3) R_C/R_A is the air-corrected He isotope ratio based on Hilton (1996).

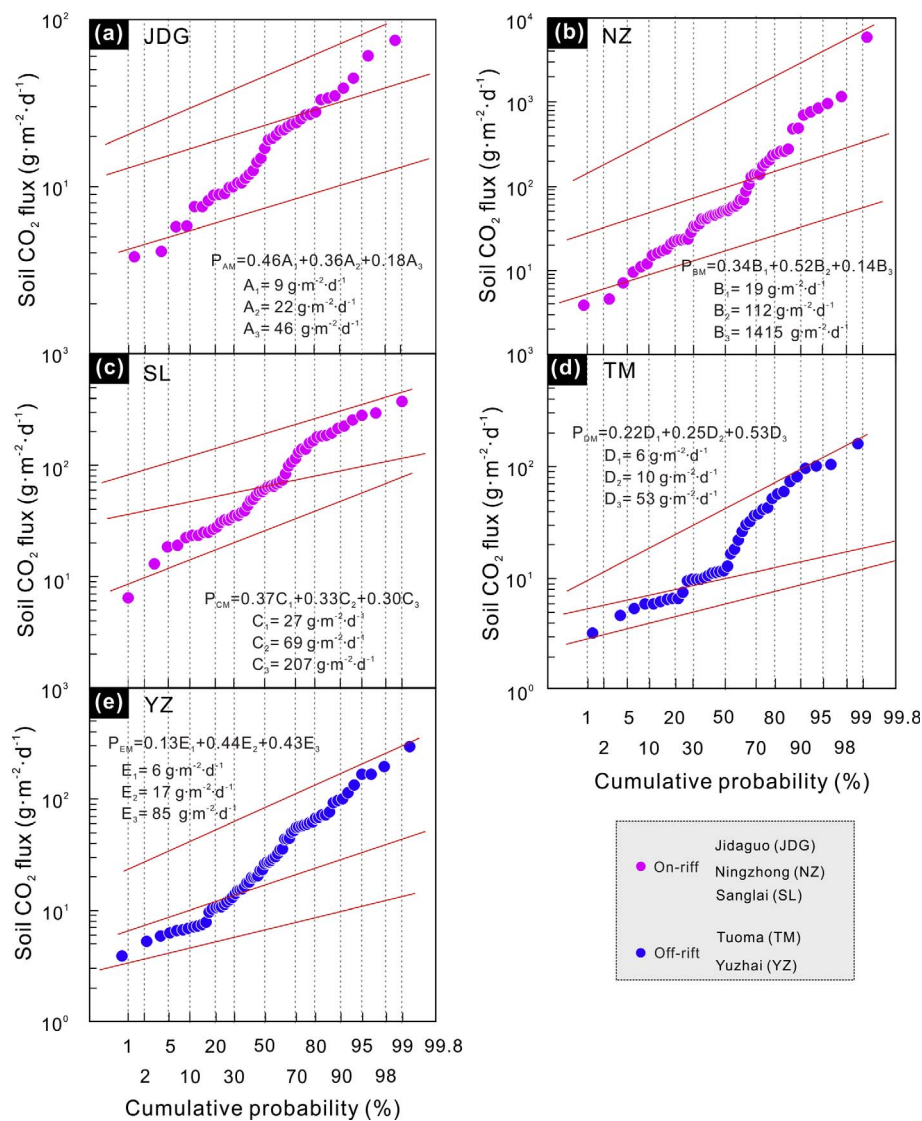


Fig. 3. Cumulative probability plot of calculated soil CO₂ fluxes for the five VGFs. Dashed lines represent the partition components of Group A (A₁, A₂, A₃)-E (E₁, E₂, E₃) (red lines). (For interpretation of the references to colour in this figure legend, the reader is referred to the web version of this article.)

Detailed analysis procedures were described in Luo et al. (2014) and Zhang et al. (2015). Chemical and isotopic compositions of the volcanic-geothermal gases were presented in Tables 1 and 2. An inter-laboratory comparison of helium and carbon isotope compositions supports the good quality of data in this study (see details in Supplementary Table S2).

4. Results

4.1. Average degassing flux of soil CO₂

Based on the in-situ determination data (Supplementary Table S1), soil CO₂ flux of each measurement point (Fig. 3) was calculated following the principle of accumulation chamber method (Chiodini et al., 1998). According to the Ideal Gas Law, molar volume of the soil CO₂ has been corrected, which could eliminate errors of calculated soil CO₂ fluxes induced by differences between local atmospheric pressure and temperature of the study areas and the standard conditions (i.e., 101 kPa and 0 °C). The calculated results range in 4–61, 5–5883, 6–373, 3–160 and 4–297 g m⁻² d⁻¹ (Table 3; see details in Supplementary Table S1) for the Jidaguo, Ningzhong, Sanglai, Tuoma and Yuzhai (Fig. 1b), respectively.

Considering large variations in calculated soil CO₂ fluxes, a statistical method based on cumulative frequency distribution (Sinclair,

1974) was adopted to evaluate the background and anomalous values. As shown in Fig. 3, the determined data of each VGF can be divided into several groups by selected inflection points, indicating presence of both background and anomalous state of soil CO₂ emissions. According to statistical weight and average of the groups, we calculated average soil CO₂ fluxes of the Jidaguo, Ningzhong, Sanglai, Tuoma and Yuzhai, which are 20, 257, 94, 32 and 45 g m⁻² d⁻¹, respectively (Table 3). These values are comparable to those of typical active VGFs at convergent and divergent plate boundaries in the world (Table 4), suggesting the Tibetan VGFs are an intensely releasing CO₂ source at the continent subduction zone at present.

4.2. Total soil CO₂ output

As suggested by conceptual model in Chiodini et al. (2008, 2015), soil CO₂ emissions in the VGFs are generally fed by gases from two types of source: (1) the biogenic source characterized by low soil CO₂ fluxes (e.g., 0.2–21 g m⁻² d⁻¹; Chiodini et al., 2008), i.e., the background source, and (2) the volcanic-geothermal source characterized by high soil CO₂ fluxes, i.e., the endogenous source. Following this criteria, carbon emissions from regions without influence of hydrothermal anomalies can be attributed to the background source, while the endogenous source indicates close affinities with hydrothermal anomalies. Considering the distributions of hydrothermal activities and related

Table 3
Estimated parameters and partitioned populations in five surveyed areas and total diffuse CO₂ output of the northern segment of GYR.

Field no.	Field	Area (km ²)	Population	Proportion (%)	Sample quantity	Average soil CO ₂ flux and 95% confidence interval (g m ⁻² d ⁻¹)	Total diffuse CO ₂ output and 95% confidence interval (t a ⁻¹)	Data source	
2	Yangying	1.5	A (background)	59	24	12 (10–15)	3905 (3058–4751)	Zhang et al. (2017b)	
			B (endogenous)	34	14	103 (58–108)	19,266 (10,880–20,106)		
			C (endogenous)	7	3	775 (360–1189)	31,041 (14,439–47,643)		
			Total	100	41	99	5.42 × 10 ⁴		
3	Jidaguo	0.5	A1 (background)	46	18	9 (8–10)	751 (642–859)	This study	
			A2 (background)	36	14	22 (20–24)	1462 (1329–1595)		
			A3 (endogenous)	18	7	46 (34–58)	1505 (1113–1897)		
			Total	100	39	20	3.72 × 10 ³		
4	Yangbajing-A	2	A (background)	12	8	1 (0.7–1.2)	85.8 (63–109)	Zhang et al. (2014)	
			B (background)	64	42	5 (4.8–6.2)	2573 (2246–2900)		
			C (background)	24	16	13 (11–15)	2302 (1914–2691)		
			Total	100	66	7	4.96 × 10 ³		
4	Yangbajing-B	2.25	A (background)	9	9	4.4 (4.1–4.8)	328 (299–357)	Zhang et al. (2014)	
			B (endogenous)	79	76	63 (51–75)	40,682 (32,965–48,400)		
			C (endogenous)	12	11	441 (280–603)	39,884 (25,298–54,470)		
			Total	100	96	99	8.09 × 10 ⁴		
6	Ningzhong	0.5	B1 (background)	34	20	19 (15–23)	1184 (927–1441)	This study	
			B2 (endogenous)	52	31	112 (16–139)	10,717 (1516–13,400)		
			B3 (endogenous)	14	8	1415 (57–2676)	35,006 (1403–66,219)		
			Total	100	59	257	4.69 × 10 ⁴		
8	Sanglai	0.64	C1 (background)	37	19	27(23–30)	2313 (1979–2646)	This study	
			C2 (endogenous)	33	17	69 (60–79)	5390 (4640–6140)		
			C3 (endogenous)	30	15	207 (173–242)	14,256 (11,903–16,609)		
			Total	100	51	94	2.2 × 10 ⁴		
10	Gulu	0.26	A (background)	36	9	12 (5–19)	409 (169–649)	Zhang et al. (2017b)	
			B (endogenous)	32	8	152 (100–203)	4612 (3049–6175)		
			C (endogenous)	32	8	1199 (932–1467)	36,431 (28,316–51,370)		
			Total	100	25	437	4.15 × 10 ⁴		
11	Tuoma	1.5	D1 (background)	22	9	6 (5–6.5)	705 (615–794)	This study	
			D2 (background)	25	10	10 (9.5–11)	1393 (1296–1491)		
			D3 (endogenous)	53	21	53 (37–69)	15,289 (10,622–19,956)		
			Total	100	40	32	1.74 × 10 ⁴		
14	Yuzhai	4.5	E1 (background)	13	9	6 (5.5–7)	1345 (1194–1497)	This study	
			E2 (background)	44	30	17(15–20)	12,631 (10,849–14,413)		
			E3 (endogenous)	43	29	85 (64–107)	59,697 (44,803–74,592)		
			Total	100	68	45	7.37 × 10 ⁴		
		2560	On-rift (background)				13 (11–14)		1.18 × 10 ⁷ (1.05 × 10 ⁷ –1.31 × 10 ⁷)
			On-rift (endogenous)				219 (149–289)		3.19 × 10 ⁶ (2.17 × 10 ⁶ –4.22 × 10 ⁶)
			Off-rift (background)				13 (11–15)		
			Off-rift (endogenous)				72 (57–86)		
Total CO ₂ output of the northern GYR		2600					1.50 × 10 ⁷ (1.27 × 10 ⁷ –1.73 × 10 ⁷)		

For the area of the endogenous-derived CO₂ (~40 km²), we follow the principles proposed by previous studies (Werner et al., 2008; Hutchison et al., 2015), which are (1) the distribution of the fault, and (2) the distribution of the hydrothermal manifestation (Liu, 2014). Following Armijo et al. (1986), the length of the rift is about 260 km and its width is about 10 km, which yields total degassing area of 2600 km² for the northern segment of GYR. Hence, the area of the background-derived CO₂ is 2560 km².

faults (i.e., uprising pathways of the CO₂-rich hydrothermal fluids), we estimated area of the endogenous region of the studied VGFs is about ~40 km² (Table 3), and that of the background region is ~2560 km² (Table 3).

Based on the calculated average soil CO₂ flux of background and endogenous regions, together with the estimated area, total soil CO₂ output of the northern GYR is about 1.50 × 10⁷ t a⁻¹ (with 95% confidence interval ranging from 1.27 × 10⁷ to 1.73 × 10⁷ t a⁻¹; Table 3). The total soil CO₂ output from the northern GYR will add new data to database of global geological carbon degassing. Compared with the total soil CO₂ output (1.76 × 10⁷ t a⁻¹; Zhang et al., 2017b) that was based on 228 measurement points of in-situ soil CO₂ emissions in three VGFs (Table 3), we suggest that the relatively lower total soil CO₂

output in this study (i.e., 1.50 × 10⁷ t a⁻¹; Table 3) represents an update to the earlier estimated value. This is because: (1) the soil CO₂ flux survey in this study covers more VGFs and thus has more measurement points relative to the previous work (Table 3), which will give rise to an updated average soil CO₂ flux; (2) the estimated area of soil micro-seepage in this study is based on the classification of background and endogenous regions, while the previous work only takes the influence of major faults into account for area estimating (as the case in Newell et al., 2008). Therefore, we suggest that similar studies should be carried out in future, which will update the knowledge of deep carbon degassing from extensional rift systems in the India-Asia continent subduction zone.

Table 4
Soil CO₂ emission rates observed in GYR and other volcanic-geothermal areas of the world.

Location	Soil CO ₂ flux (g m ⁻² d ⁻¹)	Total CO ₂ output (t a ⁻¹)	Date	Reference
Jidaguo, China	20.4	3.72 × 10 ³	2015.07	This study
Ningzhong, China	257	4.69 × 10 ⁴	2015.07	This study
Sanglai, China	94.0	2.20 × 10 ⁴	2015.07	This study
Tuoma, China	31.8	1.74 × 10 ⁴	2015.07	This study
Yuzhai, China	44.9	7.37 × 10 ⁴	2015.07	This study
Yangying, China	99.0	5.42 × 10 ⁴	2012.07–08	Zhang et al. (2017b)
Gulu, China	437	4.15 × 10 ⁴	2012.07–08	Zhang et al. (2017b)
Yangbajing-A, China	6.70	4.89 × 10 ³	2012.07–08	Zhang et al. (2014)
Yangbajing-B, China	98.5	8.09 × 10 ⁴	2012.07–08	Zhang et al. (2014)
Yangbajin, China	43.1	5.00 × 10 ⁴	1998	Chiodini et al. (1998)
Tengchong, China	280	4.43 × 10 ⁶	2015.03	Zhang et al. (2016)
Tengchong, China	25.1–875	7.00 × 10 ⁶	2012–2013	Cheng et al. (2014)
Changbaishan, China	19.4	7.79 × 10 ⁵	2012.09	Zhang et al. (2015)
Yellowstone, USA	410	1.50 × 10 ⁵	2006	Werner et al. (2008)
Mammoth Mountain, USA	218–3500	n.d.	2008	Lewicki et al. (2008)
Liu-Huang-Ku, Taiwan	582	7.80 × 10 ³	2004	Lan et al. (2007)
Liu-Huang-Ku, Taiwan	659	8.20 × 10 ³	2006	Lan et al. (2007)
Latera, Italy	3.10	1.28 × 10 ⁵	2003.10	Chiodini et al. (2007)
Ustica Italy	94.0	2.60 × 10 ⁵	1998	Etiopie et al. (1999)
Hakkoda Japan		2.70 × 10 ⁴	1999.09	Hernández Perez et al. (2003)

4.3. Chemical compositions

Bubble gas samples are generally characterized by high contents of CO₂ (81.1–97.4%), except for the N₂-rich samples XM1501 and XM1502 (southernmost samples reported in Fig. 1b; N₂, 89.9–91.4%, CO₂, 0.65–0.83%, O₂, 0.05–0.06%; Table 1). It is noted that such high CO₂ contents are corresponding to the high soil CO₂ flux of GYR (Table 3), while the low O₂ contents (< 3.0%) have indicated no air contamination during collecting samples (Rouilleau et al., 2015). The N₂/Ar ratios of the CO₂-rich samples range from 34.2 to 99.8 (Fig. 4a; Table 1), which are mainly ranging between air (N₂/Ar = 83.6; Marty et al., 1991) and air-saturated water (ASW, N₂/Ar = 38; Hamme and Emerson, 2004), indicating air mixed during the gases rising to the surface. While for the N₂/Ar ratios which are higher than air value of 83.6, may indicate excess nitrogen (e.g., crustal-derived nitrogen, mantle-derived nitrogen) adding to the samples (Table 1).

CO₂/³He ratios for CO₂-rich bubbling gases range between 2.99 × 10⁹ and 8.95 × 10¹² (Table 2; Fig. 4b), which are higher than the values of depleted mid-ocean ridge basalt (MORB)-source mantle (1.49 × 10⁸–8.30 × 10⁹; Lupton et al., 2015 and reference therein) and arc-related volcanic-geothermal fluids at ocean subduction zone

(2.20 × 10⁹–4.55 × 10¹⁰; Hilton et al., 2002; Lupton et al., 2015), suggesting significant contributions from crustal materials. Two N₂-rich samples have low CO₂/³He ratios (ranging from 6.45 × 10⁶ to 1.15 × 10⁷; Table 2) and extremely high helium content (9813–9821 ppm), implying their different source from CO₂-rich samples.

4.4. He and C isotope compositions

The measured helium isotopic ratios (R_M) range from 0.04 R_A to 1.02 R_A (where R_A = 1.39 × 10⁻⁶ is the ³He/⁴He ratios in air; Fig. 5), which have much wider range and higher values than those in the literature (0.11–0.38 R_A; Yokoyama et al., 1999; Hoke et al., 2000; Zhang et al., 2017b). Ratios of ⁴He/²⁰Ne range from 0.81 to 1146 (Table 2). It is noted that the lower ⁴He/²⁰Ne values which are close to the air (0.32; Sano et al., 1989) and ASW (0.29; Ozima and Podosek, 1983) values indicate a significant admixture of air-derived helium and/or ASW-derived helium (Table 2). In consideration of scarcely air contamination during sampling due to low O₂ contents, the atmosphere-derived helium might dissolve in the water during the groundwater uprising to the earth surface. Therefore, ASW-correction of the measured helium ratios

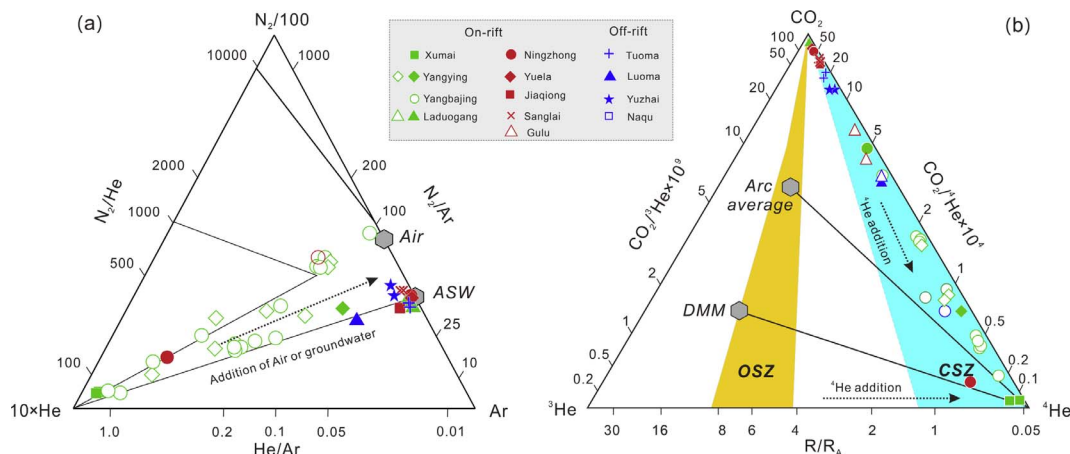


Fig. 4. Triangle plot of N₂-He-Ar (a) and CO₂-³He-⁴He (b) (modified from Taran (2011) and Lan et al. (2007)) for the volcanic-geothermal gases in GYR. Abbreviations are as follows: ASW, air-saturated water; Arc average, arc-related volatiles (³He/⁴He = 5.4 ± 1.9 R_A, Hilton et al., 2002; CO₂/³He = 4.5–29 × 10⁹, Marty et al., 1989); DMM, depleted MORB-source mantle (³He/⁴He = 8.0 ± 1.5 R_A, Sano and Fischer, 2013; CO₂/³He = 2 × 10⁹, Marty and Jambon, 1987); OSZ, ocean subduction zone; CSZ, continent subduction zone. (N₂/Ar)_{Air} = 83.6 (Marty et al., 1991) and (N₂/Ar)_{ASW} = 38 (Hamme and Emerson, 2004). The range of ocean subduction zone (OSZ) is from Lupton et al. (2015) and reference therein. Data are from this study and the published data of Zhao et al. (2002), Yokoyama et al. (1999) and Hoke et al. (2000). Filled (this study) and open symbols (previous studies) represent, respectively.

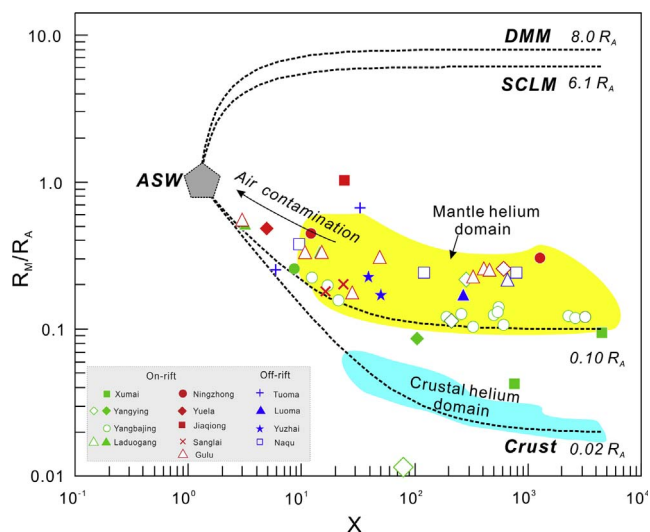


Fig. 5. $^3\text{He}/^4\text{He}$ (R_M/R_A) vs. X (the detailed calculation procedure for X is described in the footnote of Table 2) for the volcanic-geothermal gases in GYR. Calculated binary mixing curves between air saturated water (ASW), upper mantle (DMM) and sub-continental lithospheric mantle (SCLM) and crust are shown. Endmember compositions are as follows: ASW, $^3\text{He}/^4\text{He} = 1 R_A$, $^4\text{He}/^{20}\text{Ne} = 0.29$ (Ozima and Podosek, 1983); DMM, $^3\text{He}/^4\text{He} = 8.0 \pm 1.5 R_A$ (Sano and Fischer, 2013); SCLM, $^3\text{He}/^4\text{He} = 6.1 R_A$ (Gautheron and Moreira, 2002); Crust, $^3\text{He}/^4\text{He} = 0.02 R_A$ (Lupton, 1983). $^4\text{He}/^{20}\text{Ne}$ ratios ($X = 1000$) of DMM, SCLM and crust are assumed. Mantle and crustal helium domains of South Tibet are from Hoke et al. (2000). Data are from this study and literatures of Yokoyama et al. (1999) and Hoke et al. (2000).

(ASW, $^3\text{He}/^4\text{He} = 1 R_A$, $^4\text{He}/^{20}\text{Ne} = 0.29$; Ozima and Podosek, 1983) has been performed following the correction method proposed by Hilton (1996).

Combined with the helium isotopic ratios in this study and previous studies (Yokoyama et al., 1999; Hoke et al., 2000; Zhang et al., 2017b), the ASW-corrected helium ratios (0.04–1.02 R_A ; Table 2) are much higher than the continent crustal value (0.02 R_A , Lupton, 1983), showing significant mantle helium contribution (Crossey et al., 2009). The ratios are much lower than those from the depleted mid-ocean ridge basalt (MORB) mantle (DMM, $8.0 \pm 1.5 R_A$; Sano and Fischer, 2013) and subcontinental lithospheric mantle (SCLM, $6.10 \pm 0.9 R_A$; Gautheron and Moreira, 2002).

$\delta^{13}\text{C}_{\text{CO}_2}$ values in the CO_2 -rich samples range from -9.05% to 0.10% (Table 2), which are consistent those in the arc-related volatiles (-9.80% to -1.30% ; Sano and Marty, 1995; Zhang et al., 2016 and reference therein). While low $\delta^{13}\text{C}_{\text{CO}_2}$ (-14.8% and -14.6%) are observed in N_2 -dominated samples in the Xumai (Table 2), possibly implying a potential source of oxidizing sedimentary organic matter ($-30 \pm 10\%$; Hoefs, 2009).

5. Discussion

5.1. Controlling factors of soil CO_2 emissions

During early stage of lithospheric extension, rift zones in continental orogens usually exhibit high surface heat flow values related with rise of geotherm (Fig. 6a and b), in contrast to regions in early stage of lithospheric compression (Furlong and Chapman, 2013). The GYR generated by lithospheric extension in Late Miocene (12–5 Ma; Harrison et al., 1995; Yin and Harrison, 2000; Wang et al., 2014) would have high heat flow values, as supported by recent study (Fig. 6c; Jiang et al., 2016) and field observation of hydrothermal activities (Fig. 2). The estimated total soil CO_2 output ($1.50 \times 10^7 \text{ t a}^{-1}$) suggests that extensional rifts such as the GYR are significant windows of deep carbon emissions in the India-Asia continent subduction zone. More specifically, the tectonic setting of GYR could exert influence on the intensities of soil CO_2 emissions, as suggested by the substantial

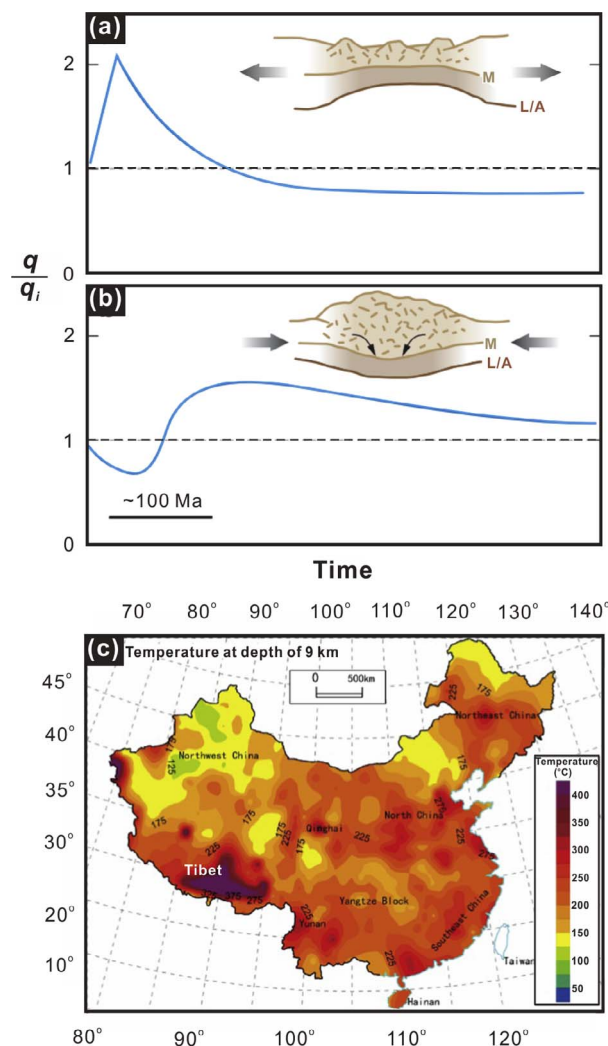


Fig. 6. Schematic models of the transient thermal effects of orogenesis: (a) heat flow response to extensional/rifting tectonics and crustal thinning and (b) heat flow response to convergent tectonics and mountain building accompanied by crustal thickening (Furlong and Chapman, 2013). Each orogeny modifies the crustal heat production distribution. The parameter q/q_i shows the surface heat flow as a multiple of the initial heat flow q_i prior to the orogenic event. Abbreviations: L/A, lithosphere/asthenosphere boundary; M, Moho. (c) Temperature distribution of the enhanced geothermal system (EGS) resource base of continental China (Jiang et al., 2016). (d) Distributions of average soil CO_2 fluxes of the VGFs along GYR. (e) Cross-section map along 92°E . BNS, Bangong-Nujiang suture; ITS, Indus-Tsangpo suture; JF, Jiali faults. The black lines show the inferred faults. The dashed white lines show the possible upwelling channel for deep hot materials. R1 to R5 are the imaged resistivity bodies from south to north, whereas C1 is the conductor (Xie et al., 2016). (f) This cartoon cross section illustrates one interpretation of the processes operating in the crust and mantle beneath Tibet (Tilmann et al., 2003; Wang et al., 2016; Xie et al., 2016). MBT, main boundary thrust; MCT, main central thrust; STD, southern Tibet detachment; JRS, Jinsha River suture; KLF, Kunlun Fault. The convection cell (black circles and arrows) underneath central and northern Tibet is superimposed eastwards (Tilmann et al., 2003). The low-velocity-high-conductivity zones (LV-HCZs) in the Tibetan crust are based on the geophysical data across the Tibetan Plateau (Nelson et al., 1996; Xie et al., 2016).

variation in average soil CO_2 fluxes ($7\text{--}437 \text{ g m}^{-2} \text{ d}^{-1}$; Table 3 and Fig. 6d) of the studied VGFs.

Outgassing rates of soil CO_2 in GYR may be controlled by fault systems which could provide uprising conduits for the carbon-rich volatiles. This can be supported by higher soil CO_2 fluxes of the on-rift VGFs ($> 90 \text{ g m}^{-2} \text{ d}^{-1}$ except for JDG and YBJ-A; Fig. 6d) than those in the off-rift VGFs ($< 50 \text{ g m}^{-2} \text{ d}^{-1}$; Fig. 6d). And especially, it is clear that the on-rift VGFs have significantly higher endogenous values (with average of $219 \text{ g m}^{-2} \text{ d}^{-1}$; Table 3) relative to those of the off-rift VGFs (with average of $72 \text{ g m}^{-2} \text{ d}^{-1}$; Table 3), indicating that the spatially

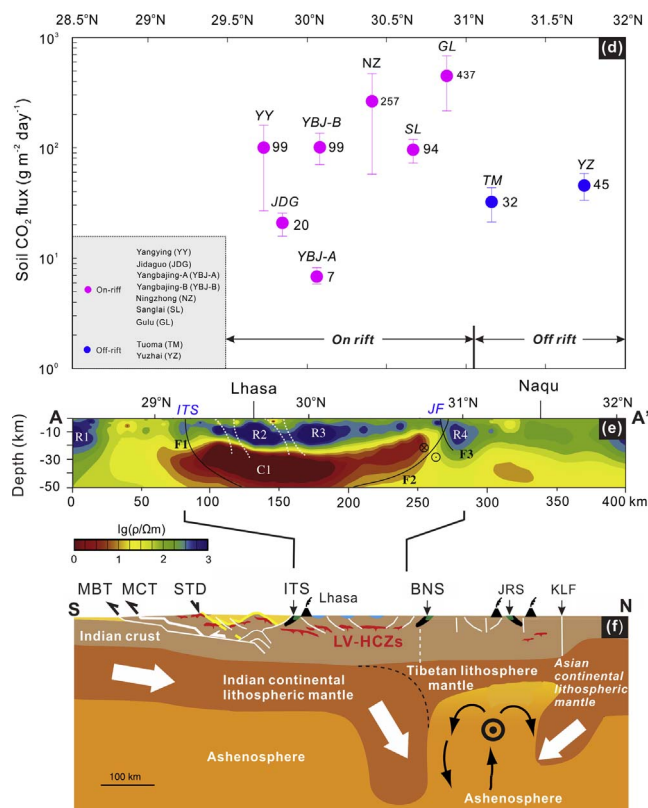


Fig. 6. (continued)

variable soil CO₂ outgassing rates may have close affinities with the fault systems. According to our field observation, the hydrothermal activities in on-rift region (Fig. 2a–f) are generally more intense than those in off-rift region (Fig. 2g–i), which is consistent with the variable soil CO₂ fluxes in the VGFs. For example, the Gulu VGF is characterized by intense hydrothermal activities (e.g., steaming fissure, geyser; Fig. 2d and e) and the highest soil CO₂ fluxes (437 g m⁻² d⁻¹; Fig. 6d). This might reflect the effects of fault system on outgassing rate of soil CO₂, because the NW-SE-trending Jiali fault transects the NE-SW-trending GYR near Gulu (Figs. 1b and 6e; Armijo et al., 1986). In contrast, there are no hydrothermal manifestation in the YBJ-A region, where fluvial sediments are abundant (Zhang et al., 2014), and thus its low average soil CO₂ flux (7 g m⁻² d⁻¹; Fig. 6d) may represent background value that has negligible contributions from the uprising carbon-rich fluids along GYR fault system. Additionally, the soil CO₂ emissions can also be affected by permeability of near-surface strata. For example, the low average soil CO₂ fluxes of the JDG in on-rift region can be explained by low permeability of thick travertine platform that impede efficient transportation of volatiles from deep source to surface.

Another controlling factor of soil CO₂ emissions is the deep source of materials and heat which has close affinities with the distribution and intensity of surface hydrothermal activities. Geophysical studies (Nelson et al., 1996; Tilmann et al., 2003; Xie et al., 2016) have revealed the presence of low-velocity-high-conductivity zones (LV-HCZs) in crustal depth beneath GYR (ca. 29–31°N; Fig. 6e and f). Combined with results of clinopyroxene-melt thermobarometer of the Late Miocene potassic volcanic rocks in GYR (Zhang et al., 2017a), the LV-HCZs are corresponding to occurrence of the crustal assimilation and fractional crystallization (AFC) process, which reflect a mantle-crust interaction and supply continuous heat and materials for the overlying hydrothermal system. It is clear that the higher average soil CO₂ fluxes (> 90 g m⁻² d⁻¹; Fig. 6d) generally occur in the on-rift region above the LV-HCZs (Fig. 6e), whereas the off-rift VGFs away from the LV-HCZs have relatively lower average soil CO₂ fluxes (< 50 g m⁻² d⁻¹; Fig. 6d

and e). Therefore, the contrasting status of soil CO₂ emissions may reflect the location of source region.

As discussed above, soil CO₂ emissions of the studied VGFs in South Tibet can be well linked to regional tectonic setting (e.g., source and fault) in the Indian-Asian continent subduction zone. However, the genesis of deep carbon degassing needs to be further constrained. In the following section, we will discuss origin and evolution of the volcanic-geothermal volatiles on the basis of the geodynamic setting of the Indian continent subduction.

5.2. Origin of the volcanic-geothermal volatiles

Compared with typical crustal-derived volatiles (0.02 R_A; Lupton, 1983), the volcanic-geothermal volatiles in the northern GYR are characterized by excess mantle-derived ³He (i.e., ³He/⁴He > 0.1 R_A; Figs. 5 and 7a). Previous studies proposed that the Tibetan mantle-derived melts or fluids could account for high ³He/⁴He ratios of hydrothermal volatiles in the India-Asia continent subduction zone (Hoke et al., 2000; Klempner et al., 2013). Additionally, the excess mantle ³He emissions have been considered to be supplied by partial melts derived from an enriched mantle wedge (EMW) source (Zhang et al., 2016, 2017c), which is consistent with the geodynamic setting of the Indian continent subduction beneath South Tibet (e.g., Nábělek et al., 2009; Guo et al., 2013, 2015; Chen et al., 2015; Shi et al., 2016). In this study, we prefer the EMW source for origin of the hydrothermal volatiles from northern GYR, and emphasize that recycling of the Indian continent materials would lead to variations in degree of mantle wedge enrichment in the north-south direction.

5.2.1. Nature of the EMW source dominated by silicate-related mantle enrichment

According to Sr-Nd-Pb isotope systematics of the post-collisional K-rich magmas (Guo et al., 2013, 2015), the metasomatic agents of mantle wedge enrichment beneath the South Tibet have been inferred to be the subducted Indian continent materials, which could be best exemplified by the silicate-dominated HHCS (i.e., the higher Himalayan crystalline sequence; Guo et al., 2013). The HHCS-derived melts and/or fluids would react with peridotite of the mantle wedge (represented by DMM) and give rise to pyroxenite (i.e., the EMW source), which has been proposed as a source lithology of the K-rich mafic magmas in South Tibet (Guo et al., 2015). During formation of the EMW source, both carbon (including organic and inorganic carbon) and radiogenic helium can be transported into the mantle wedge (Manning et al., 2013; Ague and Nicolescu, 2014; Cook-Kollars et al., 2014; Sverjensky et al., 2014; Collins et al., 2015; Liu et al., 2015; Rosenthal et al., 2015; Dai et al., 2016; Piccoli et al., 2016), leading to modification of the He-C isotope systematics (i.e., ³He/⁴He and δ¹³C) of the mantle wedge.

Combined with northward subducting of the Indian continent lithosphere, we suggest that binary mixing between the silicate-dominated HHCS components and DMM would generate an EMW source that is theoretically heterogeneous. Namely, the EMW source in the south may result from higher degree of mantle enrichment (e.g., lower ³He/⁴He and δ¹³C; Fig. 7a and b) due to higher amounts of recycled HHCS components. In contrast, the EMW source in the north probably experienced lower degree of mantle enrichment (e.g., higher ³He/⁴He and δ¹³C; Fig. 7a and b) as a result of lower amounts of recycled HHCS components. The above inference is in agreement with the ⁸⁷Sr/⁸⁶Sr evidence for a heterogeneous mantle source of the K-rich mafic magmas in the N-S-trending Xuruco-Dangreyongcuo rift (XDR, Fig. 7c; Guo et al., 2013), South Tibet.

5.2.2. He-C isotope coupling model of the EMW source

On the basis of the above discussion, we quantitatively constrained He-C isotope compositions of the EMW source using He-C isotope coupling model (Fig. 8a and b), which takes the silicate-dominated HHCS components into account for enrichment of mantle wedge

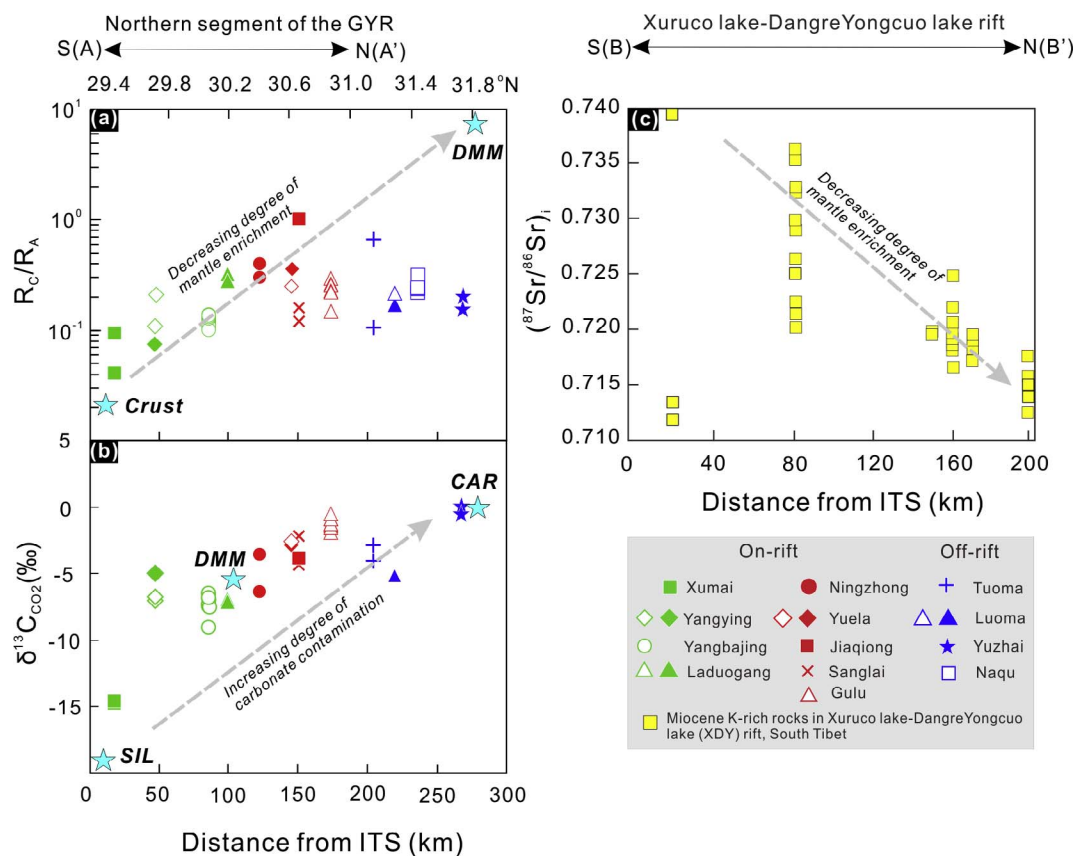


Fig. 7. R_C/R_A (a) and $\delta^{13}C_{CO_2}$ (b) for the volcanic-geothermal gases in GYR and Sr isotopes of Miocene K-rich rocks in the Dangre-Yongcuo rift, South Tibet (c) versus distance (km) from ITS. DMM (depleted MORB mantle), $^3He/^4He = 8.0 \pm 1.5 R_A$ (Sano and Fischer, 2013), $\delta^{13}C = -6.5 \pm 2.5\%$ (Pineau and Javoy, 1983); Crust, $^3He/^4He = 0.02 R_A$ (Lupton, 1983); CAR (carbonate), $\delta^{13}C = 0 \pm 2\%$ (Hoefs, 2009); SIL (silicate), $^3He/^4He = 0.02 R_A$ (Lupton, 1983), $\delta^{13}C = -21 \pm 2\%$ (Hoefs and Touret, 1975; Hans Wedepohl, 1995; Zheng et al., 2000, 2003 and reference therein). The dashed-line arrow illustrated in (a) indicates a theoretical trend line of decreasing degree of mantle enrichment from south to north along GYR, while the dashed-line arrow illustrated in (b) indicates a theoretical trend line of increasing degree of carbonate contamination from south to north along GYR. Due to the crustal contamination played a significant impact on the volatiles, the elevating trends delineated by $^3He/^4He$ isotopic ratios of the volatiles in the on-rift system cannot be directly considered to be related to decrease degree of mantle source enrichment. The samples in (a) and (b) are from this study and the published data of Yokoyama et al. (1999) and Hoke et al. (2000), and data in (c) are from Guo et al. (2013, 2015).

beneath South Tibet. Similar to volatile recycling model of ocean subduction zone (Sano and Marty, 1995), the endmembers involved in formation of the EMW source beneath South Tibet are asthenospheric

mantle (DMM), silicate (SIL) and carbonate (CAR).

The recycled SIL and CAR components can be provided by subducted HHCS (e.g., gneisses, migmatites, eclogite, carbonates and

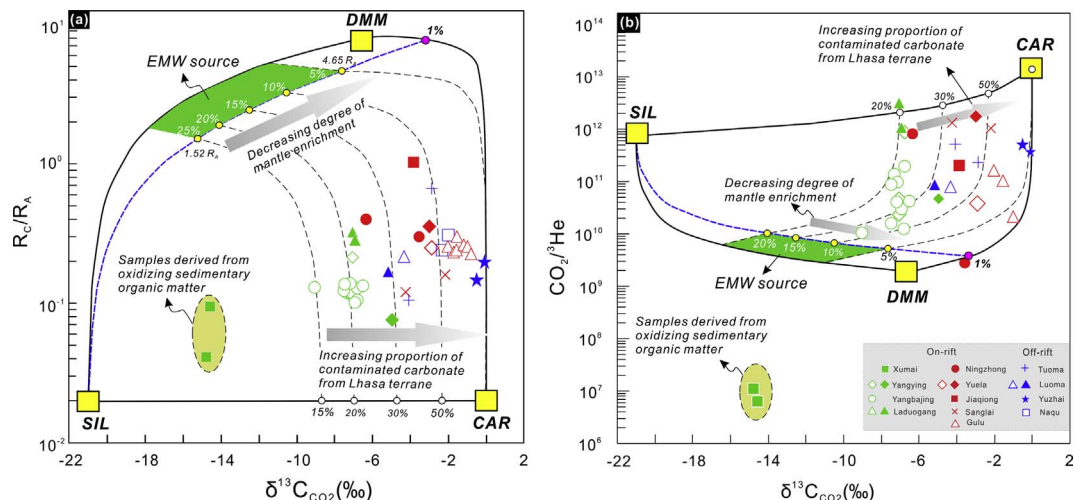


Fig. 8. He-C isotope coupling model including (a) R_C/R_A vs. $\delta^{13}C_{CO_2}$ and (b) $CO_2/^3He$ vs. $\delta^{13}C_{CO_2}$ showing mantle wedge enrichment and crust contamination for the volatiles in GYR. Abbreviations: DMM, depleted MORB mantle; CAR, subducted (HHCS-CAR) and contaminated crustal carbonate (LSC-CAR); SIL, subducted (HHCS-SIL) and contaminated crustal carbonate (LSC-SIL); EMW, enriched mantle wedge; LSC, Lhasa terrane crust. Endmember compositions are as follows, DMM: $^3He/^4He = 8.0 \pm 1.5 R_A$ (Sano and Fischer, 2013), $\delta^{13}C = -6.5 \pm 2.5\%$ (Pineau and Javoy, 1983), $CO_2/^3He = 2 \times 10^9$ (Marty and Jambon, 1987); CAR: $^3He/^4He = 0.02 R_A$ (Lupton, 1983); $\delta^{13}C = 0 \pm 2\%$ (Hoefs, 2009); $CO_2/^3He = 1.73 \times 10^{13}$ (Table 5); SIL: $^3He/^4He = 0.02 R_A$ (Lupton, 1983); $\delta^{13}C = -21 \pm 2\%$ (Hoefs and Touret, 1975; Hans Wedepohl, 1995; Zheng et al., 2000, 2003 and reference therein) and $CO_2/^3He = 8.61 \times 10^{11}$ (Table 5). The samples are from this study and the published data of Yokoyama et al. (1999) and Hoke et al. (2000).

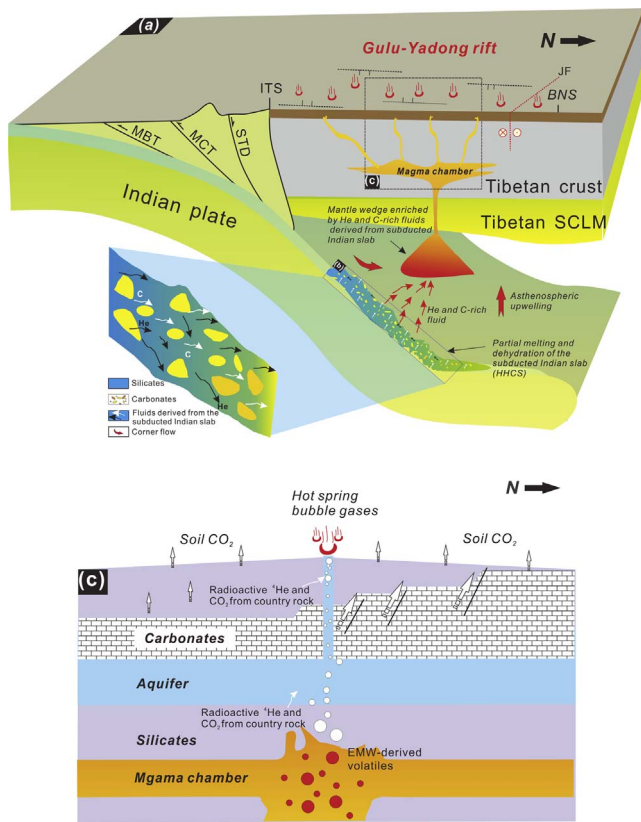


Fig. 9. (a) Genetic model of the volcanic-geothermal gases in GYR, South Tibet. The schematic map showing the formation of the EMW in a thin asthenospheric mantle wedge located beneath the Tibetan as a result of northward subduction of Indian continental; Abbreviations are as follows: BNS, Bangong-Nujiang suture; ITS, Indus-Tsangpo suture; MBT, main boundary thrust; MCT, main central thrust; STD, southern Tibetan detachment; SCLM, subcontinental lithospheric mantle; JF, Jiali fault. (b) Formation of He-rich and C-rich fluids derived from partial melting and dehydration of the subducted Indian crustal material. (c) Crustal contamination and CO_2 releasing from the VGFs in GYR (modified from Iacono-Marziano et al. (2009)). Arrows indicated CO_2 migration through rocks in permeable zones.

metasedimentary rocks; Singh et al., 1998; Pan et al., 2004; Richards et al., 2005), which are characterized by low $^3\text{He}/^4\text{He}$ and variable $\delta^{13}\text{C}_{\text{CO}_2}$ values. Specifically, we take the average $\delta^{13}\text{C}$ value of global metamorphic rocks ($-21 \pm 2 \text{‰}$; Hoefs and Touret, 1975; Hans Wedepohl, 1995; Zheng et al., 2000, 2003 and reference therein) as that of the recycled silicate rocks; the CAR endmember can be represented by recycled Precambrian carbonates from the Himalayas (Singh et al., 1998), and their $\delta^{13}\text{C}$ values theoretically vary in a range of $0 \pm 3 \text{‰}$ (Shields and Veizer, 2002; Hoefs, 2009). Following assumption in Van Soest et al. (1998), both siliceous and carbonate endmembers have $^3\text{He}/^4\text{He}$ ratio that equals the bulk continental crust value ($0.02 R_A$; Lupton, 1983). The DMM endmember has $^3\text{He}/^4\text{He}$ ratio of $8.0 \pm 1.5 R_A$ (Sano and Fischer, 2013) and $\delta^{13}\text{C}$ value of $-6.5 \pm 2.5 \text{‰}$ (Pineau and Javoy, 1983). Partition coefficients of C (0.00033; Rosenthal et al., 2015) and He (0.00017; GERM website <https://earthref.org/>) are used when calculating He and C contents of the HHCS-derived melts or fluids, which could act as metasomatic agents for mantle wedge enrichment between Indian and Asian plates (Fig. 9a and b). Other reasonable ranges of compositional parameters used in the He-C isotope modeling are shown in Table 5.

As a result of recycling of the HHCS components into mantle wedge, the EMW source would have variable $^3\text{He}/^4\text{He}$, $\delta^{13}\text{C}_{\text{CO}_2}$ and $\text{CO}_2/{}^3\text{He}$ (Fig. 8a and b), compared with the mantle wedge prior to enrichment processes. Mixing proportions of the SIL components (i.e., 5%, 10%, 15%, 20% and 25%; Fig. 8a) are based on genesis of the post-collisional K-rich mafic magmas in XDR, South Tibet (Guo et al., 2013). The effects of recycled CAR components are assumed to be negligible (e.g., < 1%;

Table 5

He and C concentration and $\delta^{13}\text{C}$ (‰) and $^3\text{He}/^4\text{He}$ (R_A) of the High Himalayan Crystalline Sequence (HHCS) and contaminated Lhasa terrane crustal endmember.

Endmember	DMM	HHCS		Lhasa terrane	
		Carbonate (CAR)	Silicate (SIL)	Carbonate (CAR)	Silicate (SIL)
U (ppm)	0.055	0.68	1.3	0.68	1.3
Th (ppm)	0.145	1.4	5.6	1.4	5.6
C (ppm)	1920	198,746	24,781	16,000	1990
$\text{C}/{}^3\text{He}$	2×10^9	1.7×10^{13}	8.16×10^{11}	1.7×10^{13}	8.16×10^{11}
He (ppm)	0.0288	0.1404	0.3642	0.0113	0.0292
$\delta^{13}\text{C}$ (‰)	-6.5	0	-21	0	-21
$^3\text{He}/^4\text{He}$ (R_A)	8	0.02	0.02	0.02	0.02

(1) $\delta^{13}\text{C}$ (‰) and $^3\text{He}/^4\text{He}$ (R_A) values of DMM are taken from Pineau and Javoy (1983) and Sano and Fischer (2013). He-C isotopic ratios of CAR and SIL of the Lhasa terrane crust are assumed to be identical to those of HHCS. $^3\text{He}/^4\text{He}$ (R_A) values of the continental crust are from Lupton (1983). $\delta^{13}\text{C}$ (‰) values of the CAR are from Hoefs (2009), while $\delta^{13}\text{C}$ (‰) isotopic ratios of the SIL are the average $\delta^{13}\text{C}$ (‰) values of eclogite and granulites (Hoefs and Touret, 1975; Hans Wedepohl, 1995; Zheng et al., 2000, 2003 and reference therein).

(2) Helium content of the SIL/CAR endmember was calculated by on the U-Th decay of the silicate rocks/carbonate rocks with age of 500 Ma (Kundig, 1989). The contents of C, U and Th for the SIL and CAR endmember of the continental crust are from Hans Wedepohl (1995), Bellanca et al. (1997), Rudnick and Gao (2003) and Lai et al. (2012). The decay constants were also shown: $\lambda^{238}\text{U} = 1.55 \times 10^{-10}$, $\lambda^{235}\text{U} = 9.85 \times 10^{-10}$, $\lambda^{232}\text{Th} = 4.95 \times 10^{-10}$. We assume $[\text{He}]_C$ equal to $[\text{He}]_{CL}$, the calculation formulas for He contents of the continental crust are presented as follows,

$$\begin{aligned}
 {}^{238}\text{U} &\xrightarrow{8\alpha+6\beta^-} {}^{206}\text{Pb} + 8{}^4_2\text{He} + 6\beta^- + E; \\
 {}^{235}\text{U} &\xrightarrow{7\alpha+4\beta^-} {}^{207}\text{Pb} + 7{}^4_2\text{He} + 4\beta^- + E; \\
 {}^{232}\text{Th} &\xrightarrow{6\alpha+4\beta^-} {}^{208}\text{Pb} + 6{}^4_2\text{He} + 4\beta^- + E
 \end{aligned}$$

Helium concentrations

$[\text{He}]_C = ((8 \times ({}^{238}\text{U}/{}^{238}) \times (e^{238\text{U}t-1}) + 7 \times ({}^{235}\text{U}/{}^{235}) \times (e^{235\text{U}t-1}) + ({}^{232}\text{Th}/{}^{232}) \times (e^{232\text{Th}t-1})) \times 4$;
According to the genesis of the EMW-source derived K-rich magma (Guo et al., 2013), we assume the degree of partial melting of HHCS (F) equals to 1%; then following batch partial melting (Wilson, 1989) and partition coefficients of C ($D_C = 0.00033$; Rosenthal et al., 2015) and He ($D_{\text{He}} = 0.00017$; this value is from the GERM Web site (<https://earthref.org/>)) we calculate the abundance of C and He adding to the mantle source. The calculation formulas for the abundance of C and He are presented:
 $[\text{He}]_{CL}/[\text{He}]_{CO} = 1/(F + D_{\text{He}} - FD_{\text{He}})$; $[\text{C}]_{CL}/[\text{C}]_{CO} = 1/(F + D_C - FD_C)$.

Fig. 8), because the K-rich mafic magmas point to a silicate-dominated EMW source (Guo et al., 2013, 2015). The calculated $^3\text{He}/^4\text{He}$ ratios of the EMW source are ranging from $1.52 R_A$ to $4.65 R_A$, which correspond to $\delta^{13}\text{C}_{\text{CO}_2}$ values from -15.3‰ to -7.65‰ and $\text{CO}_2/{}^3\text{He}$ ratios from 5.45×10^9 to 1.05×10^{10} , respectively (Fig. 8). Moreover, the EMW source exhibits a decreasing trend in degree of mantle wedge enrichment (i.e., increasing $^3\text{He}/^4\text{He}$ and $\delta^{13}\text{C}$ coupled with decreasing $\text{CO}_2/{}^3\text{He}$) from south to north, which agrees with mantle source properties of the K-rich mafic magmas in the XDR (Fig. 7c; Guo et al., 2013). Considering the additional effects of crustal contamination (see details in Section 5.2.3), we noted that the GYR samples are all enclosed by mixing curves between the EMW source and crustal materials (Fig. 8), suggesting that the EMW source could account for He-C systematics of the hydrothermal volatiles in the South Tibet.

5.2.3. Contributions from crustal components to the volcanic-geothermal volatiles

Crustal contamination must be a process accounting for differentiation of the mantle-derived volatiles during their transportation from source region to surface (Rouletau et al., 2015; Tardani et al., 2016), particularly for volatiles rising through the thickened Tibetan crust. Silicate rocks (e.g., granitoids) and carbonate rocks (e.g., sedimentary limestones) pervasively outcrop along GYR (Kidd et al., 1988; Kapp et al., 2005; Coulon et al., 1986), and are likely to be country rocks of the volcanic-geothermal system. Due to interaction between recharging meteoric water and country rocks, the hydrothermal fluids

would be enriched in radiogenic ^4He and CO_2 and act as the contaminants for EMW-derived volatiles.

During the crustal contamination process, the helium and carbon isotopic ratios of the SIL and CAR endmembers in continental crust of the Lhasa terrane are assumed to be identical to those of recycled crustal materials from the subducted Indian slab (Table 5). The best-fit mixing curves between the EMW source and crustal materials indicate that the GYR samples can be well explained by crustal contamination (Fig. 8). And more importantly, the proportion of the CAR components (e.g., 15%, 20%, 30%, 50%, 100%; Fig. 8) in the crustal endmember appears to increase from south to north (Fig. 8). Namely, the CAR components involved in contamination of samples in the south (e.g., the Yangbajing samples) are less than those of samples in the north (e.g., the Gulu and Yuzhai samples). This is consistent with the increasing $\delta^{13}\text{C}$ values (from -9.05‰ to 0.10‰) from south to north of the volcanic-geothermal volatiles of the GYR (Fig. 7b). The carbonate from the Lhasa terrane playing an increasing role from south to north along the northern GYR (Figs. 8a and 9c), implies the transition of lithology from silicate to carbonate along GYR, which is in accordance with the distribution of the crustal lithologies of the rift.

5.3. Genetic model of deep carbon emissions in the northern GYR

On the basis of origin and evolution of the GYR samples, together with constraints from petrogeochemical and geophysical studies, we propose a two-stage model to account for deep carbon emissions in the northern GYR, which highlights the important roles of the Indian continent subduction and magma-carbonate processes interaction (Iacono-Marziano et al., 2009; Deegan et al., 2010; Carter and Dasgupta, 2015) in carbon outgassing from extensional rift systems in continent subduction zone.

For the first stage, an EMW source beneath South Tibet was formed in response to northward subduction of the Indian continental lithosphere (e.g., Chen et al., 2015; Shi et al., 2016) and subsequent slab-mantle interaction (Fig. 9a and b), i.e., mixing between mantle wedge and the HHCS-derived melts and/or fluids. The feasibility of an EMW source beneath South Tibet is supported by petrogenesis of the post-collisional K-rich volcanic rocks (Guo et al., 2013, 2015) and geophysical studies that suggest the presence of a narrow mantle wedge between the Indian and Asian plates (Zhou and Murphy, 2005; Shi et al., 2016). As a result of reduce in the India-Asia convergent rate (Lee and Lawver, 1995), the subducting Indian slab experienced rollback and caused partial melting of the EMW source (Guo et al., 2013). Ascent of the EMW-derived melts, together with AFC process in the crustal depth, would lead to formation of the magma chamber beneath the GYR (as suggested by the geophysically detected LV-HCZs; Xie et al., 2016), which can provide heat energy and volatiles for the surface VGFs (Fig. 9a).

For the second stage, we suggest that the interaction between the crustal magma chamber and surrounding carbonate plays an important role in deep carbon emissions from the northern GYR (Fig. 9c). At present, the high-temperature magma chamber is continuously heating the underground aquifer and its country rocks (e.g., limestones), which would liberate radiogenic ^4He and CO_2 into the hydrothermal fluids. As suggested by the He-C coupling model (Fig. 8), the EMW-derived volatiles underwent contamination by the hydrothermal fluids during their rising from the source region, which ultimately leads to outgassing of the CO_2 -rich volatiles into the atmosphere (Fig. 9c). Therefore, our genetic model indicates that the CO_2 released from the northern GYR may be mainly supplied by sedimentary limestones in the Lhasa terrane.

6. Conclusion

Soil CO_2 emissions surveys in this study and previous studies reveal a substantial range of average soil CO_2 fluxes ($7\text{--}437\text{ g m}^{-2}\text{ d}^{-1}$) for

the on-rift and off-rift VGFs, which may have close affinities with the influence of regional fault systems and the distance to source region of heat and materials. Total soil CO_2 output of the northern GYR is about $1.50 \times 10^7\text{ t a}^{-1}$, suggesting high CO_2 outgassing flux of the VGFs in extensional rifts of the India-Asia continent subduction zone. As indicated by the He-C isotope coupling model, together with constraints from petrogeochemical and geophysical studies, the mantle-derived volatiles are attributed to an EMW source that may exhibit decreasing degrees of mantle wedge enrichment from south to north, which is consistent with the northward decreasing amounts of silicate-dominated HHCS components involved in formation of the EMW source. On the basis of crustal contamination processes, we suggest that the sedimentary carbonate rocks in the Lhasa terrane, which are heated by the EMW-derived melts beneath the GYR, play as the dominant source of the carbon released from the VGFs in the extensional rifts.

Acknowledgement

This study was supported by a grant from the Strategic Priority Research Program (B) of Chinese Academy of Sciences (Grant No. XDB03010600), grants from the National Natural Science Foundation of China (NSFC) (Nos.: 41572321 and 41602341). We are grateful to Drs. Liwu Li, Zhongping Li, Chunhui Cao Xiangxian Ma and lab technician Lantian Xing and Xibin Wang for their assistance in laboratory. Drs. Guodong Zheng, and Ching Chou Fu are thanked for helpful discussion. Reviewers are acknowledged for their extremely constructive reviews of an earlier version of the paper.

Appendix A. Supplementary material

Supplementary data associated with this article can be found, in the online version, at <http://dx.doi.org/10.1016/j.jseas.2017.05.036>.

References

- Ague, J.J., Nicolescu, S., 2014. Carbon dioxide released from subduction zones by fluid-mediated reactions. *Nat. Geosci.* 7, 355–360.
- Armijo, R., Tapponnier, P., Mercier, J.L., Han, T.L., 1986. Quaternary extension in southern Tibet field observations and tectonic implications. *J. Geophys. Res.* 91, 13083–13872.
- Bellanca, A., Masetti, D., Neri, R., 1997. Rare earth elements in limestone/marlstone couplets from the Albian-Cenomanian Cison section (Venetian region, northern Italy): assessing REE sensitivity to environmental changes. *Chem. Geol.* 141, 141–152.
- Burley, J.M., Katz, R.F., 2015. Variations in mid-ocean ridge CO_2 emissions driven by glacial cycles. *Earth Planet. Sci. Lett.* 426, 246–258.
- Burton, M.R., Sawyer, G.M., Granieri, D., 2013. Deep carbon emissions from volcanoes. *Rev. Mineral. Geochem.* 75, 323–354.
- Carter, L.B., Dasgupta, R., 2015. Hydrous basalt–limestone interaction at crustal conditions: Implications for generation of ultracalcic melts and outflux of CO_2 at volcanic arcs. *Earth Planet. Sci. Lett.* 427, 202–214.
- Chen, Y., Li, W., Yuan, X., Badal, J., Teng, J., 2015. Tearing of the Indian lithospheric slab beneath southern Tibet revealed by SKS-wave splitting measurements. *Earth Planet. Sci. Lett.* 413, 13–24.
- Cheng, Z., Guo, Z., Zhang, M., Zhang, L., 2014. Carbon dioxide emissions from Tengchong Cenozoic volcanic field, Yunnan Province, SW China. *Acta Petrologica Sinica* 30, 3657–3670 (in Chinese with English abstract).
- Chiodini, G., Baldini, A., Barberi, F., Carapezza, M.L., Cardellini, C., Frondini, F., Granieri, D., Ranaldi, M., 2007. Carbon dioxide degassing at LATERA caldera (Italy): evidence of geothermal reservoir and evaluation of its potential energy. *J. Geophys. Res.* 112, B12204. <http://dx.doi.org/10.1029/2006JB004896>.
- Chiodini, G., Caliro, S., Cardellini, C., Avino, R., Granieri, D., Schmidt, A., 2008. Carbon isotopic composition of soil CO_2 efflux, a powerful method to discriminate different sources feeding soil CO_2 degassing in volcanic–hydrothermal areas. *Earth Planet. Sci. Lett.* 274, 372–379.
- Chiodini, G., Cardellini, C., Lamberti, M.C., Agosto, M., Caselli, A., Liccioli, C., Tamburello, G., Tassi, F., Vaselli, O., Caliro, S., 2015. Carbon dioxide diffuse emission and thermal energy release from hydrothermal systems at Copahue-Caviahue Volcanic Complex (Argentina). *J. Volcanol. Geoth. Res.* 304, 294–303.
- Chiodini, G., Cioni, R., Guidi, M., Raco, B., 1998. Soil CO_2 flux measurements in volcanic and geothermal areas. *Appl. Geochem.* 13, 543–552.
- Collins, N.C., Bebout, G.E., Angiboust, S., Agard, P., Scambelluri, M., Crispini, L., John, T., 2015. Subduction zone metamorphic pathway for deep carbon cycling: II. Evidence from HP/UHP metabasaltic rocks and ophiocarbonates. *Chem. Geol.* 412, 132–150.
- Cook-Kollars, J., Bebout, G.E., Collins, N.C., Angiboust, S., Agard, P., 2014. Subduction

- zoned metamorphic pathway for deep carbon cycling: I. Evidence from HP/UHP metasedimentary rocks, Italian Alps. *Chem. Geol.* 386, 31–48.
- Coulon, C., Maluski, H., Bollinger, C., Wang, S., 1986. Mesozoic and cenozoic volcanic rocks from central and southern Tibet: ^{39}Ar – ^{40}Ar dating, petrological characteristics and geodynamical significance. *Earth Planet. Sci. Lett.* 79, 281–302.
- Crossey, L.J., Karlstrom, K.E., Springer, A.E., Newell, D., Hilton, D.R., Fischer, T., 2009. Degassing of mantle-derived CO_2 and He from springs in the southern Colorado Plateau region—neotectonic connections and implications for groundwater systems. *Geol. Soc. Am. Bull.* 121, 1034–1053.
- Dai, L.Q., Zheng, Y.F., He, H.Y., Zhao, Z.F., 2016. Postcollisional mafic igneous rocks record recycling of noble gases by deep subduction of the continental crust. *Lithos* 252, 135–144.
- DeCelles, P.G., Kapp, P., Quade, J., Gehrels, G.E., 2011. Oligocene-Miocene Kailas basin, southwestern Tibet: record of post-collisional upper-plate extension in the Indus-Yarlung suture zone. *Geol. Soc. Am. Bull.* 123, 1337–1362.
- Deegan, F.M., Troll, V.R., Freda, C., Misiti, V., Chadwick, J.P., McLeod, C.L., Davidson, J.P., 2010. Magma-carbonate interaction processes and associated CO_2 release at Merapi Volcano, Indonesia: insights from experimental petrology. *J. Petrol.* 51, 1027–1051.
- Donaldson, D.G., Webb, A.A.G., Menold, C.A., Kylander-Clark, A.R.C., Hacker, B.R., 2013. Petrochronology of Himalayan ultrahigh-pressure eclogite. *Geology* 41, 835–838.
- Etiopie, G., Beneduce, P., Calcara, M., Favali, P., Frugoni, F., Schiattarella, M., Smriglio, G., 1999. Structural pattern and CO_2 – CH_4 degassing of Ustica Island, Southern Tyrrhenian basin. *J. Volcanol. Geoth. Res.* 88, 291–304.
- Furlong, K.P., Chapman, D.S., 2013. Heat flow, heat generation, and the thermal state of the lithosphere. *Annu. Rev. Earth Planet. Sci.* 41, 385–410.
- Gautheron, C., Moreira, M., 2002. Helium signature of the subcontinental lithospheric mantle. *Earth Planet. Sci. Lett.* 199, 39–47.
- Graham, D.W., 2002. Noble gas isotope geochemistry of mid-ocean ridge and ocean island basalts: characterization of mantle source reservoirs. *Rev. Mineral. Geochem.* 47, 247–319.
- Guo, Z., Wilson, M., Liu, J., 2007. Post-collisional adakites in south Tibet: products of partial melting of subduction-modified lower crust. *Lithos* 96, 205–224.
- Guo, Z., Wilson, M., Zhang, M., Cheng, Z., Zhang, L., 2013. Post-collisional, K-rich mafic magmatism in South Tibet: constraints on Indian slab-to-wedge transport processes and plateau uplift. *Contrib. Miner. Petrol.* 165, 1311–1340.
- Guo, Z., Wilson, M., Zhang, M., Cheng, Z., Zhang, L., 2015. Post-collisional ultrapotassic mafic magmatism in South Tibet: products of partial melting of pyroxenite in the mantle wedge induced by roll-back and delamination of the subducted Indian continental lithosphere slab. *J. Petrol.* 56, 1365–1406.
- Guynn, J.H., Kapp, P., Pullen, A., 2006. Tibetan basement rocks near Amdo reveal “missing” Mesozoic tectonism along the Bangong suture, central Tibet. *Geology* 34, 505–508.
- Hacker, B., Luffi, P., Lutkov, V., Minaev, V., Ratschbacher, L., Plank, T., Ducea, M., Patiño-Douce, A., McWILLIAMS, M., Metcalf, J., 2005. Near-ultrahigh pressure processing of continental crust: Miocene crustal xenoliths from the Pamir. *J. Petrol.* 46, 1661–1687.
- Hamme, R.C., Emerson, S.R., 2004. The solubility of neon, nitrogen and argon in distilled water and seawater. *Deep Sea Res. Part I* 51, 1517–1528.
- Hans Wedepohl, K., 1995. The composition of the continental crust. *Geochim. Cosmochim. Acta* 59, 1217–1232.
- Harrison, T.M., Coperland, P., Kidd, W.S.F., Lovera, O.M., 1995. Activation of the Nyainqentanghla shear zone: implications for uplift of the southern Tibetan Plateau. *Tectonics* 14, 658–676.
- Hernández Perez, P., Notsu, K., Tsurumi, M., Mori, T., Ohno, M., Shimoike, Y., Salazar, J., Pérez, N., 2003. Carbon dioxide emissions from soils at Hakkoda, north Japan. *J. Geophys. Res.: Solid Earth* 108 (B4), 2210.
- Hilton, D.R., 1996. The helium and carbon isotope systematics of a continental geothermal system: results from monitoring studies at Long Valley caldera (California, U.S.A.). *Chem. Geol.* 127, 269–295.
- Hilton, D.R., Fischer, T.P., Marty, B., 2002. Noble gases and volatile recycling at subduction zones. *Rev. Mineral. Geochem.* 47, 319–370.
- Hoefs, J., 2009. *Stable Isotope Geochemistry*. Springer Verlag, Berlin Heidelberg, pp. 285.
- Hoefs, J., Touret, J., 1975. Fluid inclusion and carbon isotope study from Bamble granulites (South Norway). *Contrib. Miner. Petrol.* 52, 165–174.
- Hoke, L., Lamb, S., Hilton, D.R., Poreda, R.J., 2000. Southern limit of mantle-derived geothermal helium emissions in Tibet: implications for lithospheric structure. *Earth Planet. Sci. Lett.* 180, 297–308.
- Hu, D., Wu, Z., Jiang, W., Shi, Y., Ye, P., Liu, Q., 2005. SHRIMP zircon U-Pb age and Nd isotopic study on the Nyainqentanghla Group in Tibet. *Sci. China, Ser. D Earth Sci.* 48, 1377–1386.
- Huang, F., Xu, J.F., Chen, J.L., Wu, J.B., Zeng, Y.C., Xiong, Q.W., Chen, X.F., Yu, H.X., 2016. Two Cenozoic tectonic events of N-S and E-W extension in the Lhasa Terrane: evidence from geology and geochronology. *Lithos* 245, 118–132.
- Hutchison, W., Mather, T.A., Pyle, D.M., Biggs, J., Yirgu, G., 2015. Structural controls on fluid pathways in an active rift system: a case study of the Aluto volcanic complex. *Geosphere* 11, 542–562.
- Iacono-Marziano, G., Gaillard, F., Scaillet, B., Pichavant, M., Chiodini, G., 2009. Role of non-mantle CO_2 in the dynamics of volcano degassing: the Mount Vesuvius example. *Geology* 37, 319–322.
- Italiano, F., Bonfanti, P., Ditta, M., Petrini, R., Slejko, F., 2009. Helium and carbon isotopes in the dissolved gases of Friuli region (NE Italy): geochemical evidence of CO_2 production and degassing over a seismically active area. *Chem. Geol.* 266, 76–85.
- Ji, W.Q., Wu, F.Y., Liu, C.Z., Chung, S.L., 2012. Early Eocene crustal thickening in southern Tibet: new age and geochemical constraints from the Gangdese batholith. *J. Asian Earth Sci.* 53, 82–95.
- Jiang, G., Li, W., Rao, S., Shi, Y., Tang, X., Zhu, C., Gao, P., Wang, Y., Hu, S., 2016. Heat flow, depth-temperature, and assessment of the enhanced geothermal system (EGS) resource base of continental China. *Environ. Earth Sci.* 75, 1432. <http://dx.doi.org/10.1007/s12665-016-6238-5>.
- Kapp, J.L.A., Harrison, T.M., Kapp, P., Grove, M., Lovera, O.M., Lin, D., 2005. Nyainqentanghla Shan: a window into the tectonic, thermal, and geochemical evolution of the Lhasa block, southern Tibet. *J. Geophys. Res.: Solid Earth* (1978–2012) 110.
- Kelemen, P.B., Manning, C.E., 2015. Reevaluating carbon fluxes in subduction zones, what goes down, mostly comes up. *Proc. Natl. Acad. Sci.* 112, E3997–E4006.
- Kidd, W.S.F., Pan, Y., Chang, C., Coward, M.P., Dewey, J.F., Gansser, A., Molnar, P., Shackleton, R.M., Sun, Y., 1988. Geological mapping of the 1985 Chinese-British Tibetan (Xizang–Qinghai) Plateau geotraverse route. *Philos. Trans. R. Soc. Lond. Ser. A, Math. Phys. Sci.* 327, 287–305.
- Klemperer, S.L., Kennedy, B.M., Sastry, S.R., Makovsky, Y., Harinarayana, T., Leech, M.L., 2013. Mantle fluids in the Karakoram fault: helium isotope evidence. *Earth Planet. Sci. Lett.* 366, 59–70.
- Kundig, R., 1989. Domal structures and high-grade metamorphism in the Higher Himalayan crystalline, Zaskar region, north-west Himalaya, India. *J. Metamorph. Geol.* 7, 43–55.
- Lai, X., Yang, X., Sun, W., 2012. Geochemical constraints on genesis of dolomite marble in the Bayan Obo REE–Nb–Fe deposit, Inner Mongolia: implications for REE mineralization. *J. Asian Earth Sci.* 57, 90–102.
- Lan, T., Yang, T., Lee, H., Chen, Y., Chen, C., Song, S., Tsao, S., 2007. Compositions and flux of soil gas in Liu–Huang–Ku hydrothermal area, northern Taiwan. *J. Volcanol. Geoth. Res.* 165, 32–45.
- Lee, T.Y., Lawver, L.A., 1995. Cenozoic plate reconstruction of Southeast Asia. *Tectonophysics* 251, 85–138.
- Lee, H.Y., Chung, S.L., Ji, J., Qian, Q., Gallet, S., Lo, C.H., Lee, T.Y., Zhang, Q., 2012. Geochemical and Sr–Nd isotopic constraints on the genesis of the Cenozoic Linzizong volcanic successions, southern Tibet. *J. Asian Earth Sci.* 53, 96–114.
- Lewicki, J., Fischer, M., Hilley, G., 2008. Six-week time series of eddy covariance CO_2 flux at Mammoth Mountain, California: performance evaluation and role of meteorological forcing. *J. Volcanol. Geoth. Res.* 171, 178–190.
- Liang, X., Chen, Y., Tian, X., Chen, Y.J., Ni, J., Gallegos, A., Klemperer, S.L., Wang, M., Xu, T., Sun, C., Si, S., Lan, H., Teng, J., 2016. 3D imaging of subducting and fragmenting Indian continental lithosphere beneath southern and central Tibet using body-wave finite-frequency tomography. *Earth Planet. Sci. Lett.* 443, 162–175.
- Liu, D., Zhao, Z., DePaolo, D.J., Zhu, D.C., Meng, F.Y., Shi, Q., Wang, Q., 2017. Potassic volcanic rocks and adakitic intrusions in southern Tibet: insights into mantle–crust interaction and mass transfer from Indian plate. *Lithos* 268–271, 48–64.
- Liu, Y., He, D., Gao, C., Foley, S., Gao, S., Hu, Z., Zong, K., Chen, H., 2015. First direct evidence of sedimentary carbonate recycling in subduction-related xenoliths. *Sci. Rep.* 5, 11547.
- Liu, Z., 2014. The forming mechanism of typical high-temperature geothermal systems in Nima–Naqu geothermal belt, Tibet. PhD Thesis Institute of Geology Chinese Academy of the Geological Science, Beijing, pp. 111 (in Chinese with English abstract).
- Luo, M., Huang, H., Zhang, P., Wu, Q., Chen, D., 2014. Origins of gas discharging from the Qiantang Basin in the northern Qinghai–Tibet Plateau, China: evidence from gas compositions, helium, and carbon isotopes. *J. Geochem. Explor.* 146, 119–126.
- Lupton, J., Rubin, K.H., Arculus, R., Lilley, M., Butterfield, D., Resing, J., Baker, E., Embley, R., 2015. Helium isotope, C^{13}He , and Ba–Nb–Ti signatures in the northern Lau Basin: distinguishing arc, back-arc, and hotspot affinities. *Geochem. Geophys. Geosyst.* 16. <http://dx.doi.org/10.1002/2014GC005625>.
- Lupton, J.E., 1983. Terrestrial inert gases–isotope tracer studies and clues to primordial components in the mantle. *Annu. Rev. Earth Planet. Sci.* 11, 371–414.
- Manning, C.E., Shock, E.L., Sverjensky, D., 2013. The chemistry of carbon in aqueous fluids at crustal and upper mantle conditions: experimental and theoretical constraints. *Rev. Mineral. Geochem.* 75, 109–148.
- Marty, B., Gunnlaugsson, E., Jambon, A., Oskarsson, N., Ozima, M., Pineau, F., Torssander, P., 1991. Gas geochemistry of geothermal fluids, the Hengill area, southwest rift zone of Iceland. *Chem. Geol.* 91, 207–225.
- Marty, B., Jambon, A., 1987. C^{13}He in volatile fluxes from the solid Earth: implications for carbon geodynamics. *Earth Planet. Sci. Lett.* 83, 16–26.
- Marty, B., Jambon, A., Sano, Y., 1989. Helium isotopes and CO_2 in volcanic gases of Japan. *Chem. Geol.* 76, 25–40.
- Nábělek, J., Hetényi, G., Vergne, J., Sapkota, S., Kafle, B., Jiang, M., Su, H., Chen, J., Huang, B.S., 2009. Underplating in the Himalaya–Tibet collision zone revealed by the Hi–CLIMB experiment. *Science* 325, 1371–1374.
- Nelson, K.D., Zhao, W., Brown, L., Kuo, J., Che, J., Liu, X., Klemperer, S., Makovsky, Y., Meissner, R., Mechie, J., 1996. Partially molten middle crust beneath southern Tibet: synthesis of project INDEPTH results. *Science* 274, 1684–1688.
- Newell, D.L., Jessup, M.J., Cottle, J.M., Hilton, D.R., Sharp, Z.D., Fischer, T.P., 2008. Aqueous and isotope geochemistry of mineral springs along the southern margin of the Tibetan plateau: implications for fluid sources and regional degassing of CO_2 . *Geochem. Geophys. Geosyst.* 9, Q08014.
- Ozima, M., Podosek, F., 1983. *Noble Gas Geochemistry*. Cambridge University Press.
- Pan, G., Ding, J., Yao, D., Wang, L., 2004. An Introduction of Geological Map of the Tibetan Plateau and Neighbouring Area. Chengdu Map Press, Chengdu, pp. 1–133 (in Chinese).
- Piccoli, F., Brovarone, A.V., Beyssac, O., Martinez, I., Ague, J.J., Chaduteau, C., 2016. Carbonation by fluid–rock interactions at high-pressure conditions: implications for carbon cycling in subduction zones. *Earth Planet. Sci. Lett.* 445, 146–159.
- Pineau, F., Javoy, M., 1983. Carbon isotopes and concentrations in mid-oceanic ridge basalts. *Earth Planet. Sci. Lett.* 62, 239–257.
- Richards, A., Argles, T., Harris, N., Parrish, R., Ahmad, T., Darbyshire, F., Draganits, E.,

2005. Himalayan architecture constrained by isotopic tracers from clastic sediments. *Earth Planet. Sci. Lett.* 236, 773–796.
- Resing, J.A., Lupton, J.E., Feely, R.A., Lilley, M.D., 2004. CO₂ and ³He in hydrothermal plumes: implications for mid-ocean ridge CO₂ flux. *Earth Planet. Sci. Lett.* 226, 449–464.
- Rosenthal, A., Hauri, E., Hirschmann, M., 2015. Experimental determination of C, F, and H partitioning between mantle minerals and carbonated basalt, CO₂/Ba and CO₂/Nb systematics of partial melting, and the CO₂ contents of basaltic source regions. *Earth Planet. Sci. Lett.* 412, 77–87.
- Rouilleau, E., Vinet, N., Sano, Y., Takahata, N., Shinohara, H., Ooki, M., Takahashi, H.A., Furukawa, R., 2015. Effect of the volcanic front migration on helium, nitrogen, argon, and carbon geochemistry of hydrothermal/magmatic fluids from Hokkaido volcanoes, Japan. *Chem. Geol.* 414, 42–58.
- Rudnick, R.L., Gao, S., 2003. Composition of the continental crust. *Treatise Geochem.* 3 (01), 1–64.
- Sano, Y., Fischer, T.P., 2013. The analysis and interpretation of noble gases in modern hydrothermal systems: the noble gases as geochemical tracers. *Springer* 249–317.
- Sano, Y., Marty, B., 1995. Origin of carbon in fumarolic gas from island arcs. *Chem. Geol.* 119, 265–274.
- Sano, Y., Wakita, H., 1985. Geographical distribution of ³He/⁴He ratios in Japan: implications for arc tectonics and incipient magmatism. *J. Geophys. Res.: Solid Earth* (1978–2012) 90, 8729–8741.
- Sano, Y., Wakita, H., Makide, Y., Tominaga, T., 1989. A ten-year decrease in the atmospheric helium isotope ratio possibly caused by human activity. *Geophys. Res. Lett.* 16, 1371–1374.
- Shi, D., Zhao, W., Klemperer, S.L., Wu, Z., Mechie, J., Shi, J., Xue, G., Su, H., 2016. West-east transition from underplating to steep subduction in the India-Tibet collision zone revealed by receiver-brian profiles. *Earth Planet. Sci. Lett.* 452, 171–177.
- Shields, G., Veizer, J., 2002. Precambrian marine carbonate isotope database: Version 1.1. *Geochem. Geophys. Geosyst.* 3 (6). <http://dx.doi.org/10.1029/2001GC000266>.
- Sinclair, A., 1974. Selection of threshold values in geochemical data using probability graphs. *J. Geochem. Explor.* 3, 129–149.
- Singh, S.K., Trivedi, J., Pande, K., Ramesh, R., Krishnaswami, S., 1998. Chemical and strontium, oxygen, and carbon isotopic compositions of carbonates from the Lesser Himalaya: implications to the strontium isotope composition of the source waters of the Ganga, Ghaghara, and the Indus rivers. *Geochim. Cosmochim. Acta* 62, 743–755.
- Sverjensky, D.A., Stagno, V., Huang, F., 2014. Important role for organic carbon in subduction-zone fluids in the deep carbon cycle. *Nat. Geosci.* 7, 909–913.
- Taran, Y., 2011. N₂, Ar, and He as a tool for discriminating sources of volcanic fluids with application to Vulcano, Italy. *Bull. Volcanol.* 73, 395–408.
- Tardani, D., Reich, M., Rouilleau, E., Takahata, N., Sano, Y., Pérez-Flores, P., Sánchez-Alfaro, P., Cembrano, J., Arancibia, G., 2016. Exploring the structural controls on helium, nitrogen and carbon isotope signatures in hydrothermal fluids along an intra-arc fault system. *Geochim. Cosmochim. Acta* 184, 193–211.
- Tian, X., Chen, Y., Tseng, T.L., Klemperer, S.L., Thybo, H., Liu, Z., Xu, T., Liang, X., Bai, Z., Zhang, X., Si, S., Sun, C., Lan, H., Wang, E., Teng, J., 2015. Weakly coupled lithospheric extension in southern Tibet. *Earth Planet. Sci. Lett.* 430, 171–177.
- Tilmann, F., Ni, J., INDEPTH III Seismic Team, 2003. Seismic imaging of the downwelling Indian lithosphere beneath central Tibet. *Science* 300, 1424.
- Van Soest, M., Hilton, D., Kreulen, R., 1998. Tracing crustal and slab contributions to arc magmatism in the Lesser Antilles island arc using helium and carbon relationships in geothermal fluids. *Geochim. Cosmochim. Acta* 62, 3323–3335.
- Wang, C., Dai, J., Zhao, X., Li, Y., Graham, S.A., He, D., Ran, B., Meng, J., 2014. Outward-growth of the Tibetan Plateau during the Cenozoic: a review. *Tectonophysics* 621, 1–43.
- Wang, Q., Hawkesworth, C.J., Wyman, D., Chung, S.L., Wu, F.Y., Li, X.H., Li, Z.X., Gou, G.N., Zhang, X.Z., Tang, G.J., Dan, W., Ma, L., Dong, Y.H., 2016. Pliocene-Quaternary crustal melting in central and northern Tibet and insights into crustal flow. *Nat. Commun.* 7, 11888. <http://dx.doi.org/10.1038/ncomms11888>.
- Wang, R., Richards, J.P., Zhou, L.M., Hou, Z.Q., Stern, R.A., Creaser, R.A., Zhu, J.J., 2015. The role of Indian and Tibetan lithosphere in spatial distribution of Cenozoic magmatism and porphyry Cu–Mo deposits in the Gangdese belt, southern Tibet. *Earth Sci. Rev.* 150, 68–94.
- Weiss, R.F., 1971. Solubility of helium and neon in water and seawater. *J. Chem. Eng. Data* 16 (2), 235–241.
- Weller, O., St-Onge, M., Rayner, N., Searle, M., Waters, D., 2016. Miocene magmatism in the Western Nyainqentanglha Mountains of southern Tibet: an exhumed bright spot? *Lithos* 245, 147–160.
- Werner, C., Hurwitz, S., Evans, W., Lowenstern, J., Bergfeld, D., Heasler, H., Jaworowski, C., Hunt, A., 2008. Volatile emissions and gas geochemistry of Hot Spring Basin, Yellowstone National Park, USA. *J. Volcanol. Geoth. Res.* 178, 751–762.
- Wilson, B.M., 1989. *Igneous Petrogenesis: A Global Tectonic Approach*. Unwin Hyman pp. 466.
- Xie, C., Jin, S., Wei, W., Ye, G., Jing, J., Zhang, L., Dong, H., Yin, Y., Wang, G., Xia, R., 2016. Crustal electrical structures and deep processes of the eastern Lhasa terrane in the south Tibetan plateau as revealed by magnetotelluric data. *Tectonophysics* 675, 168–180.
- Yin, A., Harrison, T.M., 2000. Geologic evolution of the Himalayan-Tibetan orogen. *Annu. Rev. Earth Planet. Sci.* 28, 211–280.
- Yokoyama, T., Nakai, S., Wakita, H., 1999. Helium and carbon isotopic compositions of hot spring gases in the Tibetan Plateau. *J. Volcanol. Geoth. Res.* 88, 99–107.
- Zhang, L., Guo, Z., Zhang, M., Cheng, Z., 2014. Study on Soil micro-seepage gas flux in the high temperature geothermal area: an example from the Yangbajing geothermal field, South Tibet. *Acta Petrologica Sinica* 30 (12), 3612–3626 (in Chinese with English abstract).
- Zhang, L., Guo, Z., Zhang, M., Cheng, Z., Sun, Y., 2017a. Post-collisional potassic magmatism in the eastern Lhasa terrane, south Tibet: products of partial melting of mélanges in a continental subduction channel. *Gondwana Res.* 41, 9–28.
- Zhang, L., Guo, Z., Zheng, G., Zhang, M., Sun, Y., Cheng, Z., Ma, X., 2017b. Flux and genesis of greenhouse gases emissions from Miocene volcanic-geothermal fields, South Tibet: a case study from Gulu and Yangying volcanic-geothermal fields. *Acta Petrologica Sinica* 33 (1), 250–266 (in Chinese with English abstract).
- Zhang, M., Guo, Z., Sano, Y., Cheng, Z., Zhang, L., 2015. Stagnant subducted Pacific slab-derived CO₂ emissions: insights into magma degassing at Changbaishan volcano, NE China. *J. Asian Earth Sci.* 106, 49–63.
- Zhang, M., Guo, Z., Sano, Y., Zhang, L., Sun, Y., Cheng, Z., Yang, T.F., 2016. Magma-derived CO₂ emissions in the Tengchong volcanic field, SE Tibet: implications for deep carbon cycle at intra-continent subduction zone. *J. Asian Earth Sci.* 127, 76–90.
- Zhang, M., Guo, Z., Zhang, L., Sun, Y., Cheng, Z., 2017c. Geochemical constraints on origin of hydrothermal volatiles from southern Tibet and the Himalayas: understanding the degassing systems in the India-Asia continental subduction zone. *Chem. Geol.* in press.
- Zhang, Y., 2014. Degassing history of Earth. *Treatise Geochem.* 2, 37–69.
- Zhang, Z., Chen, Y., Yuan, X., Tian, X., Klemperer, S.L., Xu, T., Bai, Z., Zhang, H., Wu, J., Teng, J., 2013. Normal faulting from simple shear rifting in South Tibet, using evidence from passive seismic profiling across the Yadong-Gulu rift. *Tectonophysics* 606, 178–186.
- Zhao, P., Xie, E.J., Dor, J., Jin, J., Hu, X.C., Du, S.P., Yao, Z.H., 2002. Geochemical characteristics of geothermal gases and their geological implications in Tibet. *Acta Petrologica Sinica* 18 (4), 539–550 (in Chinese with English abstract).
- Zhao, W., Kumar, P., Mechie, J., Kind, R., Meissner, R., Wu, Z., Shi, D., Su, H., Xue, G., Karplus, M., 2011. Tibetan plate overriding the Asian plate in central and northern Tibet. *Nat. Geosci.* 4, 870–873.
- Zheng, Y.F., Fu, B., Gong, B., Li, L., 2003. Stable isotope geochemistry of ultrahigh pressure metamorphic rocks from the Dabie-Sulu orogen in China: implications for geodynamics and fluid regime. *Earth Sci. Rev.* 62, 105–161.
- Zheng, Y.F., Gong, B., Li, Y., Wang, Z., Fu, B., 2000. Carbon concentrations and isotopic ratios of eclogites from the Dabie and Sulu terranes in China. *Chem. Geol.* 168, 291–305.
- Zhou, H.W., Murphy, M.A., 2005. Tomographic evidence for wholesale underthrusting of India beneath the entire Tibetan plateau. *J. Asian Earth Sci.* 25, 445–457.
- Zhu, D.C., Pan, G.T., Chung, S.L., Liao, Z.L., Wang, L.Q., Li, G.M., 2008. SHRIMP zircon age and geochemical constraints on the origin of Lower Jurassic volcanic rocks from the Yeba Formation, southern Gangdese, South Tibet. *Int. Geol. Rev.* 50, 442–471.